

# Vibration-induced drop atomization and the numerical simulation of low-frequency single-droplet ejection

By ASHLEY J. JAMES<sup>1</sup>, MARC K. SMITH<sup>2</sup>  
AND ARI GLEZER<sup>2</sup>

<sup>1</sup>Department of Aerospace Engineering and Mechanics, University of Minnesota,  
Minneapolis, MN 55455, USA

<sup>2</sup>George W. Woodruff School of Mechanical Engineering, Georgia Institute of Technology,  
Atlanta, GA 30332, USA

(Received 20 March 2001 and in revised form 20 August 2002)

Vibration-induced droplet ejection is a novel way to create a spray. In this method, a liquid drop is placed on a vertically vibrating solid surface. The vibration leads to the formation of waves on the free surface. Secondary droplets break off from the wave crests when the forcing amplitude is above a critical value. When the forcing frequency is small, only low-order axisymmetric wave modes are excited, and a single secondary droplet is ejected from the tip of the primary drop. When the forcing frequency is high, many high-order non-axisymmetric modes are excited, the motion is chaotic, and numerous small secondary droplets are ejected simultaneously from across the surface of the primary drop. In both frequency regimes a crater may form that collapses to create a liquid spike from which droplet ejection occurs. An axisymmetric, incompressible, Navier–Stokes solver was developed to simulate the low-frequency ejection process. A volume-of-fluid method was used to track the free surface, with surface tension incorporated using the continuum-surface-force method. A time sequence of the simulated interface shape compared favourably with an experimental sequence. The dynamics of the droplet ejection process was investigated, and the conditions under which ejection occurs and the effect of the system parameters on the process were determined.

---

## 1. Introduction

The atomization of liquids is important in a number of industrial processes, some of which are outlined by Frohn & Roth (2000). These include spray cooling, spray coating, mixing, material processing, and humidification. Other important uses span a wide range from aerospace applications, including atomization and injection for engine combustors, to biomedical applications, such as emulsification and encapsulation. A heat transfer cell for high-power microelectronic cooling is our current focus. In order to exploit the droplet atomization phenomenon in such processes it is important to understand how the phenomenon works and to be able to characterize it. This information is needed to optimize the design of devices such as the heat transfer cell. The goal of the present work is to help provide the required understanding of droplet ejection.

Vibration-induced droplet ejection is a novel method to create a liquid spray. In

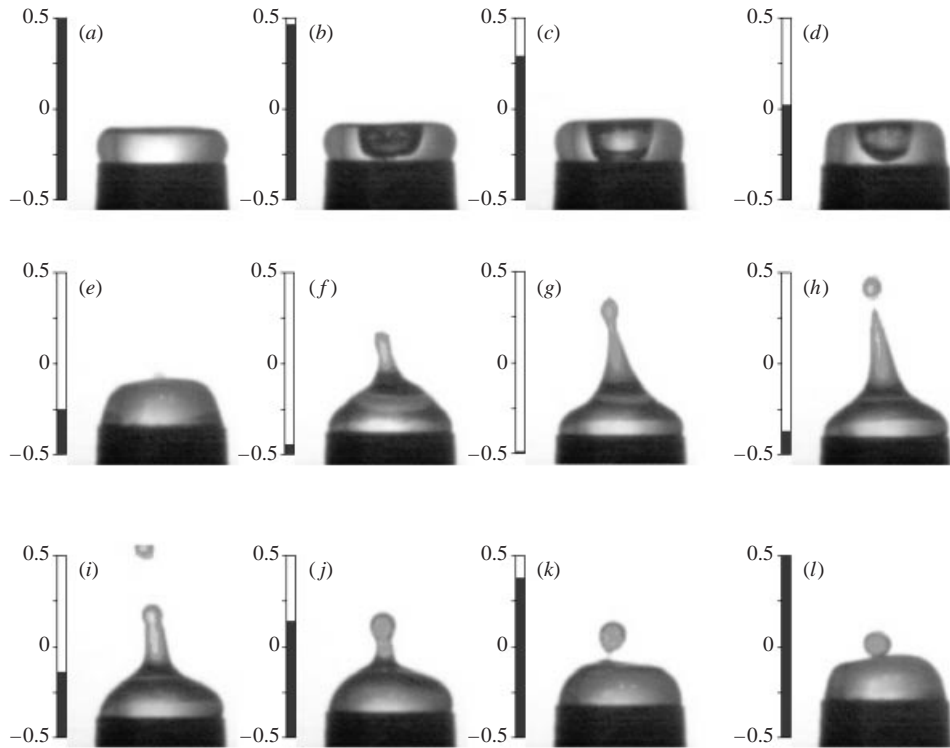


FIGURE 1. A time sequence of experimental video stills showing the drop shape. The slider bar to the left of each image indicates the displacement of the base. The fluid is water with a volume of  $30\mu\text{l}$ . The forcing parameters are a frequency of 61 Hz and an acceleration amplitude of  $66\text{ m s}^{-2}$ . Images courtesy of Dr Kai Range.

this process, a liquid drop is placed on a vertically vibrating, horizontal, solid surface. The vibration causes waves to form on the surface of the drop. When the forcing amplitude is above a threshold, secondary droplets break off from the wave crests.

The value of the forcing frequency has a dramatic effect on the process. As reported by Range, Glezer & Smith (2001), when the forcing frequency is small, only low-order, axisymmetric wave modes are excited. When the forcing amplitude is also small, the primary drop oscillates without ejection occurring. When the forcing amplitude is high enough, the upward motion of the base causes the primary drop to flatten, which leads to the formation of a crater or depression in the centre of the drop. Then, as the base moves downward, surface tension forces cause the crater to collapse towards the centre. The liquid flowing into the centre forms a high-pressure region. This forces the liquid upward, creating a high-momentum liquid spike in the centre of the drop. One or more secondary droplets may then pinch off from the end of the spike.

An example of this behaviour is shown in the time sequence of experimental images in figure 1. The liquid was water, the drop volume was  $30\mu\text{l}$ , and the forcing frequency was 61 Hz. A corresponding simulation sequence, produced using the model described in this paper, is shown in figure 2. The simulation parameters were chosen to match the experimental conditions of figure 1. The displacement of the solid base is indicated by slider bars in figure 1, and by horizontal lines in figure 2. The motion of the drop in the experiment and the simulation are slightly out of phase from one another. This

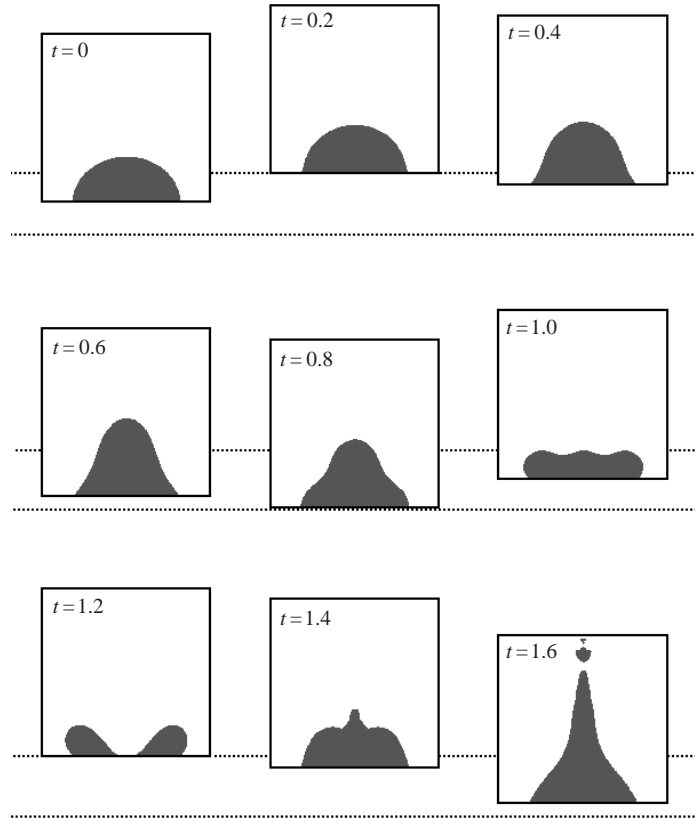


FIGURE 2. The computed drop-shape time sequence. The horizontal lines indicate the minimum and maximum displacement of the base. Time is in units of forcing periods. The problem parameters (defined in the text) are  $Re = 475$ ,  $Bo = 1.30$ ,  $A = 8.74$ ,  $\Omega = 1.24$ ,  $\theta = 0$ ,  $\alpha = 0.0012$ , and  $\beta = 0.018$ .

is due to the differing initial conditions. The forcing amplitude was ramped up in the experiment and stepped up in the simulation. In other respects the simulation and the experiment are strikingly similar. In both cases a crater formed, as seen at  $t = 1.2$  in figure 2 and in images (b)–(d) in figure 1. The crater then collapsed to form a spike in the centre of the drop, as seen at  $t = 1.4$  in figure 2 and figures 1(f) and 1(g). Finally, a secondary droplet pinched off from the end of the spike. The secondary droplet is seen at  $t = 1.6$  in figure 2 and in figures 1(h) and 1(i). Later, in figure 1(k), another droplet pinched off as the spike collapsed, but this droplet immediately fell back into the primary drop, as seen in figure 1(l).

The parameter values of the simulation of figure 2 are close to the limits of applicability of the numerical method, which is best suited to low-surface-tension, high-viscosity fluids. Given this limitation the agreement between figures 1 and 2 is quite good, although the computed shape of the ejected drop is clearly erroneous. Quantitative experimental data are not available for comparison. More rigorous verification of the numerical method, including determination of the applicability limits, is presented in §2.

Under certain conditions, when the forcing amplitude is moderate, a crater may form and collapse to enclose a bubble, as presented in §3 below. When the walls of the crater are steep the rim of the crater collapses more quickly than the bottom of the crater, so a bubble is enclosed. As in the case without a bubble, a spike is formed.

The liquid that flows inward during the crater collapse can move downward into the bubble, as well as upward to form a spike, so the momentum of the spike is smaller than if there were no bubble. Droplet ejection may or may not occur. Increasing the forcing amplitude further leads to droplet ejection without the formation of a crater. In this case the initial upward momentum of the primary drop is sufficient for droplet ejection to occur before a crater forms.

The behaviour is quite different when the forcing frequency is high. The vibratory mode observed first is generally a set of axisymmetric waves that appear as concentric circles. Other modes become active as the driving amplitude is increased, including azimuthal modes, and the response becomes chaotic. When the forcing amplitude is high enough, many secondary droplets are ejected simultaneously from across the surface of the drop. At a single ejection location on the surface of the drop, a small crater may form and then collapse to create a spike from which ejection occurs. The process of ejection from a crater is similar in the low- and high-frequency regimes. Because of this similarity, we hope that studying the low-frequency response will help elucidate the high-frequency behaviour. James *et al.* (2003) discuss the high-frequency behaviour in detail, present visualizations of the high-frequency response, including close-ups of crater formation, and describe an interesting interaction between the high-frequency ejection dynamics and the dynamics of the transducer. These authors present experimental results and a simplified model of this dynamic coupling.

The first stage of the vibration-induced atomization process, that of surface wave formation, was first reported by Faraday (1831) for a layer of liquid. Miles & Henderson (1990) have reviewed the Faraday-wave literature. The linear stability of Faraday waves was first presented by Benjamin & Ursell (1954) for inviscid fluids, and more recently, for viscous fluids, by Kumar & Tuckerman (1994), Kumar (1996), Besson, Edwards & Tuckerman (1996), and Lioubashevski, Fineberg & Tuckerman (1997). For most parameter values, the least stable mode is subharmonic. The nonlinear dynamics of Faraday waves have been studied analytically by Miles (1993), Zhang & Vinals (1997), Nayfeh & Nayfeh (1990), and Decent & Craik (1995). Giavedoni (1995) presented a nonlinear numerical simulation of Faraday waves using a finite element method. Edwards & Fauve (1994), Ciliberto & Gollub (1984, 1985), Ciliberto, Douady & Fauve (1991), Jiang *et al.* (1996), and Virnig, Berman & Sethna (1988) have performed experimental studies. Pattern formation, mode interactions, chaotic response, and hysteresis have all been investigated.

Several experimental studies of attached drop oscillations have been performed. Rodot, Bisch & Lasek (1979) reported the amplitude of the response as a function of the system parameters. Chiba & Wakamatsu (1997) determined the effect of the contact angle on the response. DePaoli, Scott & Basaran (1992) determined the first few mode shapes and the dependence of the natural frequency on the drop size. Numerical work has been done, as well. Siekmann & Schilling (1989), Gañán & Barrero (1990), and Basaran & DePaoli (1994) simulated the free oscillations of an attached drop. The resonant frequencies and mode shapes were determined. Wilkes & Basaran (1997, 1999) studied the forced oscillations of a drop hanging from a solid surface.

A few researchers have investigated the ejection of droplets due to vertical vibration. Sorokin (1957) observed droplet ejection experimentally. Goodridge, Shi & Lathrop (1996) performed experiments in which a layer of liquid was oscillated vertically and droplets were ejected from the liquid surface. The forcing amplitude threshold for droplet ejection was measured. For low-frequency forcing a smooth surface with a single liquid spike was seen. A droplet was ejected from the tip of the spike. For

high-frequency forcing a turbulent state was observed with numerous liquid spikes ejecting many droplets. In the latter case, edge effects are small because the excited wavelengths are much smaller than the size of the container. For this case, a scaling law was found for the dependence of the ejection threshold on the forcing frequency and fluid properties. Goodridge *et al.* (1997) extended the scaling law to include viscous effects. Shi, Goodridge & Lathrop (1997) studied bifurcations in the response to low-frequency forcing. They found that as the forcing amplitude was increased, the response went from stationary, to periodic, to modulated, to periodic with a response period seven times the forcing period, to ejecting, to periodic with a response period six times the forcing period, to ejecting. The ejecting states were characterized by the presence of singular fluid spikes from which droplets were ejected. Hogrefe *et al.* (1998) examined this singularity in more detail. To determine its structure, they developed a local model that predicted a power-law scaling of the interfacial shape. This scaling was confirmed by the experimental data. The spike is created by the collapse of a crater, which was studied theoretically and experimentally by Zeff *et al.* (2000). They found a similarity solution for the shape of the crater during its collapse. Yule & Al-Suleimani (2000) describe various droplet formation modes observed in their experiments on the high-frequency vibration of a liquid layer. They also present a model to explain the apparent randomness in ejection from multiple sites on the liquid surface.

The breakup of a liquid surface occurs in a number of other flows, and sometimes looks very similar to vibration-induced ejection. Examples include droplet impact, jet break-up, dripping, and cavity filling. Droplet impact is of particular interest because it can lead to splashing that has a striking resemblance to vibration-induced ejection. In both a crater may form and then collapse to create a jet from which a droplet breaks off. The impact of a drop on a solid surface was studied numerically by Fukai *et al.* (1993, 1995) and experimentally by Yarin & Weiss (1995). The impact of a drop on a liquid layer was studied numerically by Pumphrey & Crum (1988) and Pumphrey, Crum & Bjørnø (1989), and experimentally by Oguz & Prosperetti (1990). The transient interface shape was computed or visualized in each of these studies.

Jet break-up is also relevant to the present work, and has been studied extensively. The literature is reviewed by Eggers (1997). His focus is on theory, including stability, one-dimensional approximations, and similarity solutions, although computational and experimental work is also discussed. Numerical simulations of the full Navier–Stokes equations have been performed by Wilkes, Phillips & Basaran (1999) and Wilkes & Basaran (2001) using a finite element method and by Beris, Richards & Lenhoff (1996) using a volume-of-fluid method. Vibration has been used to regulate jet break-up, for example by Webster & Longmire (2001) and Chen & Basaran (2002).

In the present work, computations were performed using a volume-of-fluid (VOF) method to simulate the low-frequency droplet ejection process. This method has been used to study various processes such as jet break-up (Zhang 1999*a, b*), two-layer Couette flow (Coward *et al.* 1997), and the break-up of a drop in a shear flow (Li, Renardy & Renardy 2000). Additional simulations are presented in various papers concerning the development of, and improvements to, the numerical method, including Gueyffier *et al.* (1999), Puckett *et al.* (1997), Rudman (1997, 1998), and Renardy & Renardy (2002). The VOF method is reviewed by Scardovelli & Zaleski (1999).

The remainder of the paper is organized as follows. The computational method is described in §2, including references to the literature. The detailed dynamics of the droplet ejection process is discussed in §3. Low-frequency droplet ejection was simulated over a range of the parameters. The effects of the physical parameters on

the volume of the ejected droplet, the velocity of the ejected droplet, and the time at which ejection occurred are presented in §4. The threshold forcing amplitude, above which ejection occurs, is discussed in §5. Conclusions are presented in §6.

## 2. Computational method

An axisymmetric, Navier–Stokes solver, based on a projection method, was designed to simulate the transient fluid mechanics of low-frequency, vibration-induced, droplet ejection. In the volume-of-fluid method, a volume fraction,  $F$ , is defined in each cell as the fraction of the cell volume that contains liquid. The volume fraction is convected with the flow to track the interface. The equations are solved in both the liquid drop and the surrounding gas. Surface tension is incorporated using the continuum-surface-force (CSF) method. In this method, surface-tension forces are included directly in the momentum equation. The majority of previous work using the VOF and CSF methods is in Cartesian geometry, but Beris *et al.* (1996) successfully used these methods in an axisymmetric geometry to study jet break-up.

The axisymmetric governing equations are written in a reference frame that oscillates with the solid base. The equations are non-dimensionalized using a length scale that is the cube root of the drop volume,  $\mathcal{V}$ . The velocity scale is  $\sqrt{\sigma/\rho_L\mathcal{V}^{1/3}}$ , the time scale is  $\sqrt{\rho_L\mathcal{V}/\sigma}$ , and the pressure scale is  $\sigma/\mathcal{V}^{1/3}$ . The dimensionless density,  $\rho$ , and viscosity,  $\mu$ , are scaled on the liquid properties, denoted by a subscript  $L$ . Gas properties are denoted by a subscript  $G$ . The surface tension coefficient is  $\sigma$ . After non-dimensionalization, the governing equations are

$$\nabla \cdot \mathbf{V} = 0, \quad (1)$$

$$\rho \left[ \frac{\partial \mathbf{V}}{\partial t} + (\mathbf{V} \cdot \nabla) \mathbf{V} \right] = -\nabla p + \frac{1}{Re} \nabla \cdot (2\mu \mathbf{D}) + \rho [A \sin(2\pi\Omega t + \theta) - Bo] \hat{\mathbf{k}} + \kappa \nabla F. \quad (2)$$

The velocity is  $\mathbf{V}$ , the pressure is  $p$ , and the rate of deformation tensor is  $\mathbf{D}$ . The last term in equation (2) is from the continuum-surface-force method. It is the interfacial curvature,  $\kappa$ , times the gradient of the volume fraction. The CSF method is discussed further below. The vibratory forcing is the sine term in equation (2). The density and viscosity were assumed to be constant in each fluid, but in order to apply the same equations in every cell they were retained as variables in the equations. Thus, the density and viscosity are both linear functions of the volume fraction across the interface. The dimensionless groups are defined as follows: the Reynolds number  $Re = \sqrt{\rho_L\sigma\mathcal{V}^{1/3}}/\mu_L$ , the Bond number  $Bo = \rho_L g \mathcal{V}^{2/3}/\sigma$ , the dimensionless forcing amplitude  $A = \rho_L a \mathcal{V}^{2/3}/\sigma$ , the dimensionless forcing frequency  $\Omega = \omega \sqrt{\rho_L\mathcal{V}/\sigma}$ , the density ratio  $\alpha = \rho_G/\rho_L$ , and the viscosity ratio  $\beta = \mu_G/\mu_L$ . The dimensional forcing acceleration amplitude is  $a$  and the dimensional forcing frequency is  $\omega$ . The phase of the forcing is  $\theta$ .

The equations were discretized on a uniform, staggered grid, in a rectangular domain, using a finite-volume method. Central differencing was used on all terms, except for the convective terms, for which the hybrid differencing of Nichols, Hirt & Hotchkiss (1980) was used. The marker-and-cell (MAC) method of Harlow & Welch (1965) was used to compute the velocity and pressure fields. In this projection method, the explicitly discretized Navier–Stokes equations were advanced in time to calculate an intermediate velocity field. The divergence of the intermediate velocity was used as the source term in a Poisson equation for the pressure change. The solution of this equation was used to update the pressure to the next time step. The pressure was then

used to update the intermediate velocity to the divergence-free velocity at the next time step. The discrete Poisson equation was solved using an incomplete-Cholesky conjugate-gradient (ICCG) method. This is an iterative method with preconditioning and is presented by Golub & Van Loan (1989), Meijerink & van der Vorst (1977, 1981), and Kershaw (1978).

The initial velocity was zero in the moving reference frame, so the drop was initially translating as a rigid body with the base. The initial liquid drop shape was hemispherical and the pressure was hydrostatic. Although the drop would not be exactly hemispherical with this pressure distribution (unless there was no gravity), the hydrostatic pressure change was small compared to the capillary pressure for the parameters considered, so the gravitational modification of the drop shape would be small. The left ( $r = 0$ ) boundary was a symmetry line. The bottom and right boundaries were no-slip walls. The position of the contact line on the bottom boundary was held fixed to match the experiments of Range *et al.* (2001). In that work the solid surface was a small piston and the drop volume was chosen so that the drop filled the top of the piston, pinning the contact line at the sharp edge. Possible motion of the contact line when the contact angle is very large or very small was neglected. The top boundary was an exit plane. Liquid that left the domain through the exit plane was not allowed to re-enter.

Adaptive time stepping was used to ensure that the computation remained stable. The time step was limited by convective, diffusive, and capillary criteria as defined by Nichols *et al.* (1980):

$$\Delta t = \min \left[ C_1 \frac{\Delta r}{u_{\max}}, C_1 \frac{\Delta z}{v_{\max}}, C_2 \frac{Re \Delta r^2 \Delta z^2}{2(\Delta r^2 + \Delta z^2)} \min \left( 1, \frac{\alpha}{\beta} \right), C_3 \sqrt{\frac{\alpha}{8} \min(\Delta r, \Delta z)^3} \right]. \quad (3)$$

The Courant number,  $C_1$ , the von Neumann number,  $C_2$ , and the capillary time-step limiter,  $C_3$ , were each chosen to be less than one for numerical stability. The radial and vertical components of velocity are  $u$  and  $v$ , respectively. At every step, equation (3) was used to compute the time step,  $\Delta t$ .

The volume-of-fluid method was developed by Nichols *et al.* (1980) and Hirt & Nichols (1981). The main advantages of the method are that the free-surface shape is not constrained in any way and changes in topology are handled automatically. The interface location is tracked as it moves through the fixed, structured, Eulerian grid. In each cell the volume fraction is defined as the fraction of the cell volume that is occupied by liquid. The volume fraction is 1 in cells that contain only liquid, zero in cells that contain only gas, and between zero and 1 in cells that contain an interface. The evolution of the volume fraction is governed by the following convection equation:

$$\frac{\partial F}{\partial t} + (\mathbf{V} \cdot \nabla) F = 0. \quad (4)$$

This equation is solved in every cell, but is non-trivial only near the interface. The volume fraction is discontinuous at the interface. To maintain the discontinuous nature of  $F$  care was taken not to introduce numerical diffusion when solving equation (4). Diffusion would cause smoothing of the discontinuity and the interface would become smeared normal to itself. The approach used to avoid this was to calculate the volume fraction flux across each cell face using a linear approximation of the interface position. The fluxes were then used to update the volume fraction to the next time step.

Following the methodology of Puckett *et al.* (1997), equation (4) was split into

radial and vertical directions using an intermediate volume fraction. The fluxes were calculated in one direction and used to update the volume fraction to the intermediate level. Then, using the intermediate volume fraction, the fluxes were calculated in the other direction and used to update the intermediate volume fraction to the next time level. The direction computed first was switched at each time step. The volume fraction flux is the amount of liquid that passes through the cell face during the time step. This is equal to the amount of liquid in the domain of dependence at the beginning of the time step. The domain of dependence was approximated by the region bounded by the face of interest, the two adjacent perpendicular grid lines, and a line parallel to the face of interest that was a distance of  $U\Delta t$  away from the face in the direction opposite the direction of motion.  $U$  was the velocity normal to the face. Note that the sign of  $U$  determined which cell the domain of dependence was in and the sign of the flux. The flux was the intersection of the domain of dependence and the portion of the cell volume that contained liquid, as defined by a straight-line approximation of the interface. The line segments were defined independently in each cell, so the approximate interface need not be continuous from one cell to the next. In each partially full cell, a slope and an intercept represented the line segment. The slope of the interface was calculated from the normal vector, which is defined below. Additionally, the liquid was flagged to be above or below the line segment; this was also determined from the normal vector. The intercept was calculated iteratively to ensure that the line segment defined the correct volume fraction.

The continuum-surface-force method was introduced by Kothe, Mjolsness & Torrey (1991). It was developed for use with the volume-of-fluid method and has similar advantages: ‘The continuum method eliminates the need for interface reconstruction, simplifies the calculation of surface tension, enables accurate modeling of two- and three-dimensional fluid flows driven by surface forces, and does not impose any modeling restrictions on the number, complexity, or dynamic evolution of fluid interfaces having surface tension’ (Brackbill, Kothe & Zemach 1992). In the CSF method the surface-tension force is distributed over a thin layer near the interface to become a volume force. As the thickness of the layer approaches zero the volume force approaches the proper surface force. The continuum surface force is included in the momentum equation, so the surface-tension force is calculated in every cell, but it is non-zero only near the interface.

The interfacial curvature is computed from the volume fraction, and since the volume fraction is discontinuous at the interface the computation must be done carefully. Additionally, since the gradient of the volume fraction is non-zero only near the interface, the curvature is only defined near the interface. The volume fraction used to calculate the curvature is smoothed, also following the methodology of Brackbill *et al.* (1992). Smoothing is needed because the interfacial region is very thin. The smoothed volume fraction is only used in the curvature calculation. Once the volume fraction has been smoothed, the normal vector,  $\mathbf{n}$ , and the curvature,  $\kappa$ , are calculated from the following equations using finite-difference techniques:

$$\mathbf{n} = \nabla F, \quad (5)$$

$$\kappa = \frac{1}{|\mathbf{n}|} \left[ \left( \frac{\mathbf{n}}{|\mathbf{n}|} \cdot \nabla \right) |\mathbf{n}| - (\nabla \cdot \mathbf{n}) \right]. \quad (6)$$

This form of the curvature was found by Brackbill *et al.* (1992) to favour contributions from the centre of the interfacial region when discretized, yielding more accurate results.

Using the volume-of-fluid and continuum-surface-force methods makes it unnecessary to apply boundary conditions at the interface. The volume-of-fluid method satisfies the kinematic condition. The momentum equation satisfies the stress-balance boundary condition when the continuum surface force is included. Because of this the governing equations are the same in every cell.

Changes in topology occur naturally in this method, so there is no rupture criterion. The method tracks volumes of fluid, not the interface itself. The interface is reconstructed at each time step, but connectivity is not determined. An interface segment in a grid cell is independent of the rest of the interface. Because of this structure, the method does not pick up whether or not the interface is singly connected, or which fluid volumes are connected to one another. This is determined as part of the interpretation of the data during post-processing. In the post-processing an  $F = 1/2$  contour is drawn to represent the interface. If this contour has transitioned from being singly connected to multiply connected from one time step to the next rupture is considered to have occurred.

Consider a drop that is stretched to form a neck along the axis of symmetry. At some time the neck thins to the point where it occupies a single grid cell along the axis. Liquid is convected out of this cell through both the top and bottom cell faces, further thinning the neck. When all the liquid in the cell has been convected out of the cell rupture has occurred. Rupture generally occurs before the cell is completely emptied because the  $F = 1/2$  contour becomes disconnected.

Just before rupture the neck radius is on the order of the size of a grid cell. The details of pinch-off do not strongly affect the overall dynamics of the process, so the results we present are nevertheless valid. However, improvement of the resolution would be necessary to accurately simulate the formation of satellites, which we will consider in future work.

Extensive validation studies of our numerical algorithm were performed. The important points will be discussed presently, and the details (in addition to further details of the computational method) are given by James (2000). The pressure solver, flow solver, and volume fraction evolution routine were tested separately and together. The effects of grid resolution and all other computational parameters were evaluated for various test problems and for the vibration-induced droplet ejection problem. The effect of grid spacing on the ejected-drop velocity, ejected-drop volume, and time of ejection is shown in figure 3. It was found that the grid spacing affects the ejected-drop volume and the time of ejection weakly. The computations presented in §§ 3–5 all use a grid spacing of 0.05, which can be seen from figure 3 to be adequate.

Tests were performed to evaluate the effect of parasitic errors, which are a known limitation of the VOF/CSF method (Brackbill *et al.* 1992). An unsupported spherical drop in zero gravity is in static equilibrium. However, truncation error in the numerical method leads to motion. Under some conditions the computation becomes unstable and the drop fragments. The effect of the numerical and physical parameters on this numerical instability was quantified via the kinetic energy and an  $L_1$  measure of the error in the interface shape. Refining the grid decreased the kinetic energy and the error. Smoothing in the curvature computation was required for stability, but too much smoothing re-introduced instability. The simulation became unstable if the Reynolds number was high. For a Weber number ( $We = \rho_L U \gamma^{1/3} / \sigma$ ) of 0.01, simulations for  $Re = 1$  and  $Re = 10$  were stable, and for  $Re = 100$  were unstable. For the two stable cases, the pressure jump across the interface was 2.4% higher than the theoretical value at the end of the simulation. A case was run with water–air properties and was found to be unstable. These results provide a guideline of parameter ranges

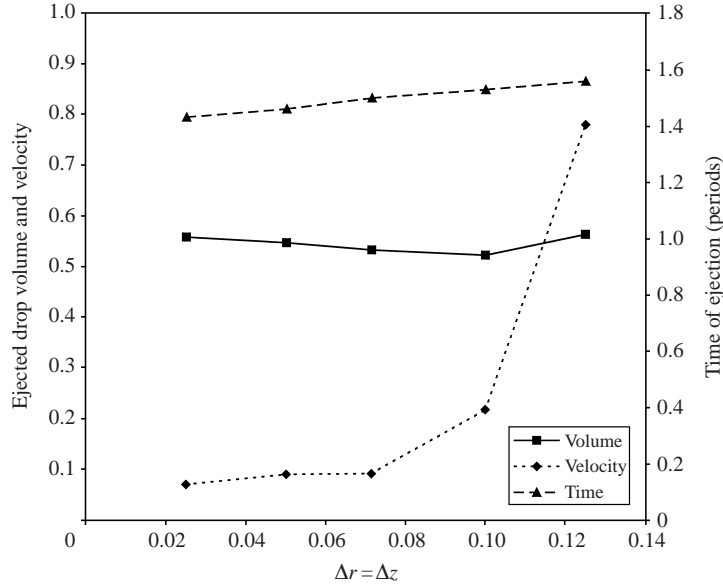


FIGURE 3. Effect of grid resolution on the response.  $Re = 10$ ,  $A = 25$ ,  $Bo = 0$ ,  $\Omega = 1$ ,  $\theta = 0$ ,  $\alpha = 0.001$ , and  $\beta = 0.001$ .

Grid cells per direction	Density ratio	$P_{drop}/P_{theory}$		$L_2$	
		Kothe	Present	Kothe	Present
16	0.5	0.70	1.004	3.904	2.827
32	0.5	0.71	0.994	1.588	1.085
16	0.1	0.84	1.010	2.255	1.487
32	0.1	0.82	0.987	1.014	1.436
16	0.001	1.32	1.008	4.130	1.580
32	0.001	1.88	0.984	4.703	1.549

TABLE 1. Comparison of static drop pressure to the results of Kothe *et al.* (1996).

for which parasitic errors may be an issue. However, the pressure errors that cause parasitic currents are small and should be less important in a situation with large physical variations in the pressure, which is the case in the droplet ejection problem.

Additional cases of the static drop problem were run to compare to the data of Kothe *et al.* (1996). They computed the pressure in a static drop and an  $L_2$  norm of the pressure distribution error for three density ratios and two grid resolutions. The  $L_2$  norm is a measure of the deviation of the computed pressure distribution from the theoretical distribution. A comparison of the present axisymmetric data to their three-dimensional data is given in table 1. All parameter values were the same. The present results are uniformly better.

Computations were performed for comparison with the computations of Wilkes & Basaran (2001). They simulated vibration-induced motion of a drop, up to the moment of break-up, using a finite element method. When the minimum radius reached 0.002 they stopped their computations and assumed break-up was imminent. The present computations were also stopped at break-up for this comparison. The only physical difference between the two simulations is that the surrounding medium is neglected

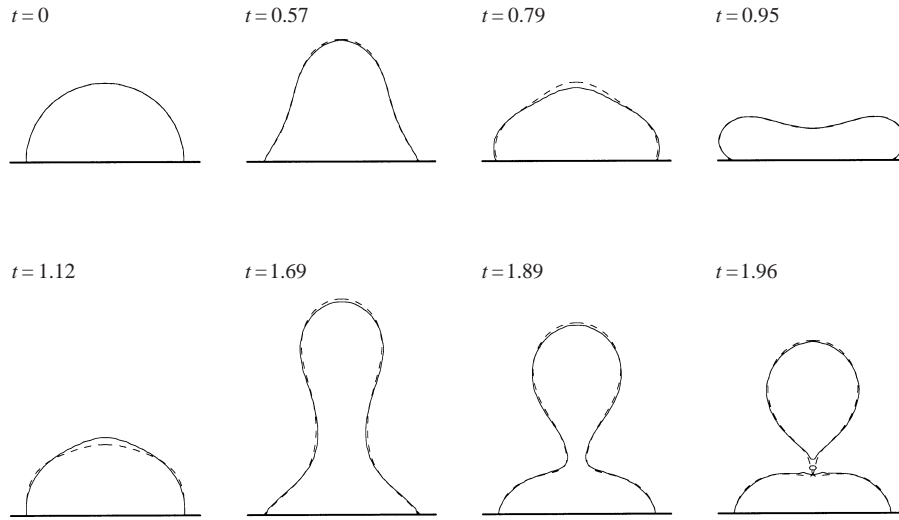


FIGURE 4. Drop shape profile evolution. Time in periods.  $Re = 22.6$ ,  $Bo = 0$ ,  $\Omega = 0.81$ ,  $A = 5.61$ ,  $\alpha = 0.001$ ,  $\beta = 0$ . Solid line: present work; dashed line: Wilkes & Basaran (2001).

by Wilkes & Basaran, but included in the present work. For this comparison the surrounding fluid viscosity was set to zero, and its density was set to 0.001 times that of the drop fluid. In figure 4 the computed interface shape from both Wilkes & Basaran and the present work are shown at several times for a forcing amplitude of  $A = 5.61$ . The length of the drop is plotted as a function of time in figure 5 for the same parameters. The two computations predict time of ejection within 0.7%, and maximum elongation within 1.3%, of one another. Another comparison was with a forcing amplitude of  $A = 5.5$ . All other parameter values remained the same. Although the forcing amplitude was decreased by only a small amount, the ejection time increased substantially, changing from the end of the second cycle to the end of the fifth cycle. This jump in ejection time is typical of the system behaviour as the amplitude is decreased. It is predicted by both the present computations and by Wilkes & Basaran, with a difference in ejection time of only 0.3%. The maximum elongation in the second cycle differs by 0.8%, and the maximum just before pinch-off differs by 3.7%, between the two computations. Overall, the results of the two computations agree very well and both predict the same large change in time of ejection for a small change in forcing amplitude.

### 3. Ejection dynamics

In order to understand the dynamics of the ejection process it is instructive to study the flow field in the drop. Two cases are considered. In both cases the Reynolds number was 10, the dimensionless driving frequency was 1, the driving phase was zero, and there was no gravity. In the first case, the driving amplitude was 25 and ejection occurred without a crater forming. In the second case, the driving amplitude was decreased to 18 and a crater formed that led to ejection. For the water–glycerin mixture used in some of our experiments these parameters correspond to a 1.24 cm drop diameter, a 10.4 Hz forcing frequency, and a 2.20 or 1.58 g forcing amplitude.

In figures 6 and 9 time sequences of the drop shape and velocity vectors are shown for the two cases with  $A = 25$  and  $A = 18$ , respectively. The horizontal lines show the

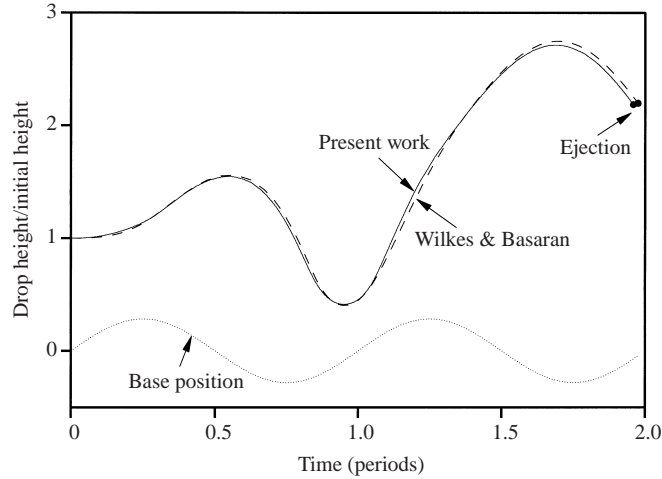


FIGURE 5. Droplet height on centreline as a function of time.  $Re = 22.6$ ,  $Bo = 0$ ,  $\Omega = 0.81$ ,  $A = 5.61$ ,  $\alpha = 0.001$ ,  $\beta = 0$ .

minimum and maximum displacements of the base. The rectangle shows the extent of the domain. The velocities, which were computed in the reference frame of the moving domain, have been transformed into a stationary reference frame. Therefore, the vectors on the bottom of the domain indicate the velocity of the solid base. The radial velocity is defined half a cell away from the bottom boundary, so in the figures it appears to be non-zero at the base even though the no-slip condition is applied there. The scales of the velocity vectors in the two figures are the same. Velocity vectors are shown only in every third computational cell for clarity. Close-ups of the neck near the time of ejection are shown in figures 7 and 10. Pressure contours are shown in figures 8 and 11 for the same cases.

First consider the case illustrated in figures 6–8. When the simulation begins, the solid base is at its midpoint and is moving upward. The drop is moving upward as a rigid body with the base velocity. During the first part of the cycle, until  $t = 0.25$ , the base is moving up, but is decelerating. The bottom of the drop must maintain the same velocity as the base, but since the drop has upward inertia the upper portion moves faster and the drop becomes elongated. A pressure maximum forms at the tip of the drop due to surface tension forces. At  $t = 0.25$  the base velocity is zero, so a stagnation point forms in the flow on the centreline.

During the next part of the cycle, until  $t = 0.75$ , the base is moving downward, and the bottom portion of the drop moves down with the base. The upper portion has enough inertia to continue to move upward, but it slows down since the bottom portion is pulling downward on it. The stagnation point separates the two regions. The stagnation point is formed at the base at  $t = 0.25$ , it moves up the axis of the drop until about  $t = 0.5$ , and then it moves down the axis of the drop. The liquid flows radially inward and vertically away from this stagnation point. Because of this flow structure the drop continues to elongate and a neck forms. There is still a local maximum in pressure at the tip, and a second local maximum forms at the neck, also due to surface tension forces. Note that although the pressure maximum occurs at the thinnest part of the neck, the stagnation point does not. A third local maximum in pressure forms at the base during this interval. At  $t = 0.75$  the base velocity is again zero, so a second stagnation point forms.

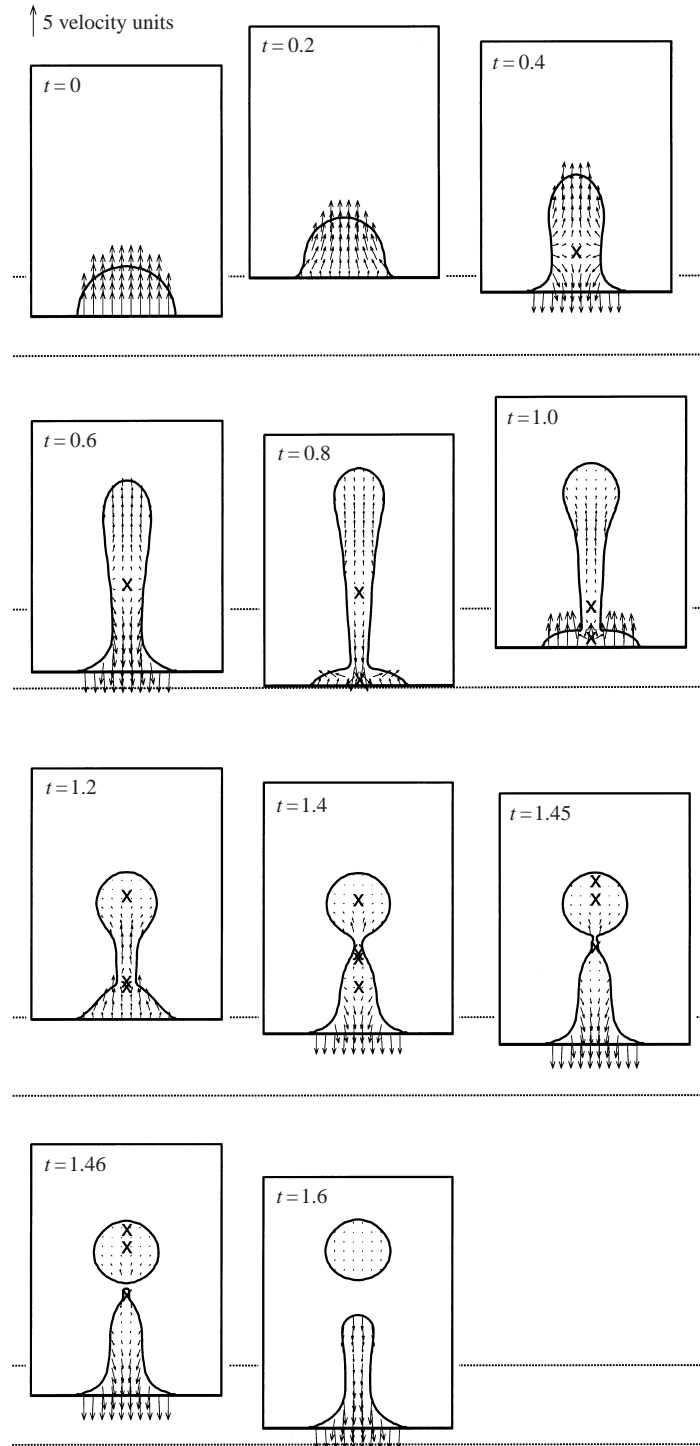


FIGURE 6. The droplet ejection process without the formation of a crater. Time is in periods. Velocity vectors are shown in every third cell. The horizontal lines indicate the minimum and maximum displacement of the base. Stagnation points are indicated by  $\times$ .  $Re = 10$ ,  $Bo = 0$ ,  $A = 25$ ,  $\Omega = 1$ ,  $\theta = 0$ ,  $\alpha = 0.001$ , and  $\beta = 0.001$ . The arrow at top left shows the velocity scale in dimensionless units.  $30 \times 80$  grid cells in half of the domain shown.

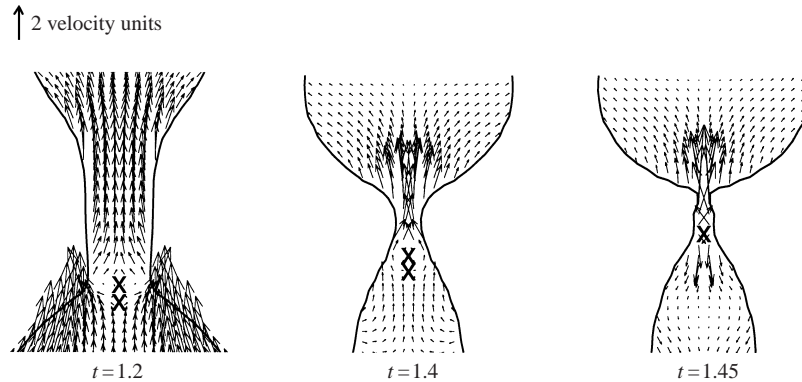


FIGURE 7. Close-up of pinch-off. Time is in periods. Velocity vectors are shown in every cell. Stagnation points are indicated by  $\times$ .  $Re = 10$ ,  $Bo = 0$ ,  $A = 25$ ,  $\Omega = 1$ ,  $\theta = 0$ ,  $\alpha = 0.001$ , and  $\beta = 0.001$ .  $30 \times 80$  grid cells.

During the next stage, from  $t = 0.75$  to  $t = 1.25$ , the base moves upward. The uppermost tip of the drop continues to move upward, then slows to a stop and reverses direction. This causes the formation of a stagnation point in the upper portion of the drop. During this interval the tip is hardly moving, but liquid is still flowing in from below. This flow, in conjunction with surface-tension forces, causes the upper region to become more spherical. The first stagnation point moves downward, and then moves upward. The lower stagnation point quickly moves up to approach the first one. The flow in the neck moves radially outward and vertically toward the lower stagnation point. This causes the liquid region near the base to thicken. All the local pressure maxima are maintained. At  $t = 1.25$  the base velocity is zero and a fourth stagnation point forms at the base of the drop.

Droplet ejection occurs during the next stage (between  $t = 1.25$  and  $t = 1.5$ ) while the base is moving down. The upper portion of the drop is nearly spherical at pinch-off. The two middle stagnation points merge just below the neck. These stagnation points are very close together for some time, as seen in figure 7, so it is difficult to resolve exactly when they merge. The pressure is high at the neck, due to surface tension. This forces liquid to flow up out of the neck, so the neck thins and pinch-off occurs. After pinch-off the lower portion of the drop quickly recoils as the base and surface tension pull it downward. The ejected droplet becomes rounder and continues to slowly move upward.

Next consider the case illustrated in figures 9–11, in which the forcing amplitude is smaller than before. The initial motion is similar to the previous case. The drop moves upward as a rigid body with the velocity of the base. As the base slows, from  $t = 0$  to  $t = 0.25$ , the inertia of the drop causes it to elongate. When the velocity of the base is zero, a stagnation point forms. As the base moves downward, from  $t = 0.25$  to  $t = 0.75$ , the upper portion of the drop moves upward and the lower portion moves downward. This causes the further elongation of the drop and the formation of a neck. The lower portion pulls on the upper portion, causing the upper portion to slow. Unlike the previous case, the upper portion slows to a stop and reverses direction. This is because the forcing amplitude is lower, so the upper portion of the drop does not have as much inertia.

The next stage of the motion, from  $t = 0.75$  to  $t = 1.25$ , is quite different from the previous case. The base is moving upward in this interval and the upper portion of

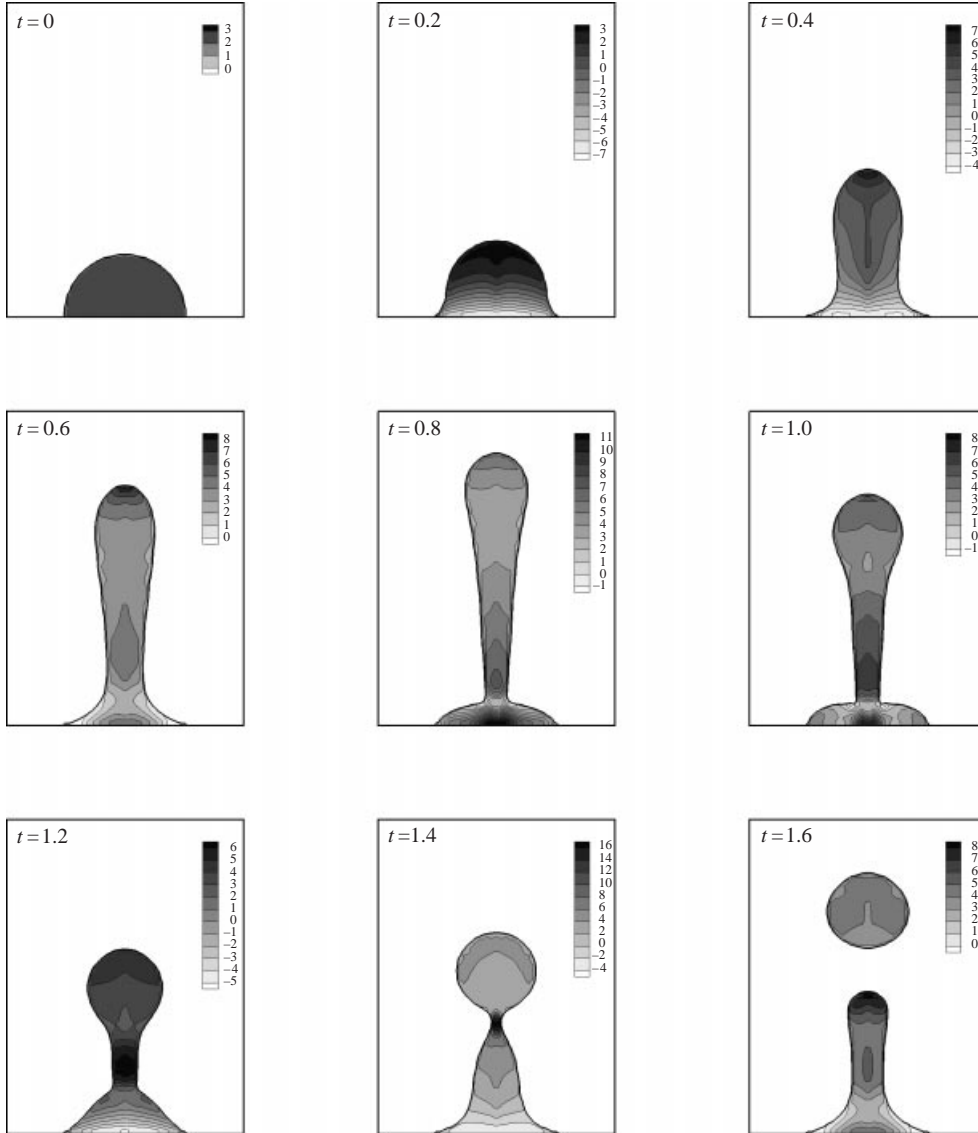


FIGURE 8. Pressure contours in the droplet ejection process without the formation of a crater. Time is in periods.  $Re = 10$ ,  $Bo = 0$ ,  $A = 25$ ,  $\Omega = 1$ ,  $\theta = 0$ ,  $\alpha = 0.001$ , and  $\beta = 0.001$ .  $30 \times 80$  grid cells in half of domain shown.

the drop is moving downward. This causes the neck to fill in. Next, from  $t = 1.25$  to  $t = 1.75$  the base moves downward. The entire drop also moves downward during this phase.

Next, from  $t = 1.75$  to  $t = 2.25$ , the base moves upward. The drop initially has momentum downward, but is restrained by the upward motion of the base. This causes the downward momentum to be transferred into outward, radial momentum. This is seen as flattening of the drop. The centre of the drop thins to form a crater.

As the base slows down after  $t = 2$ , and then reverses direction at  $t = 2.25$ , the crater begins to collapse. Large surface tension forces due to the negative curvature of

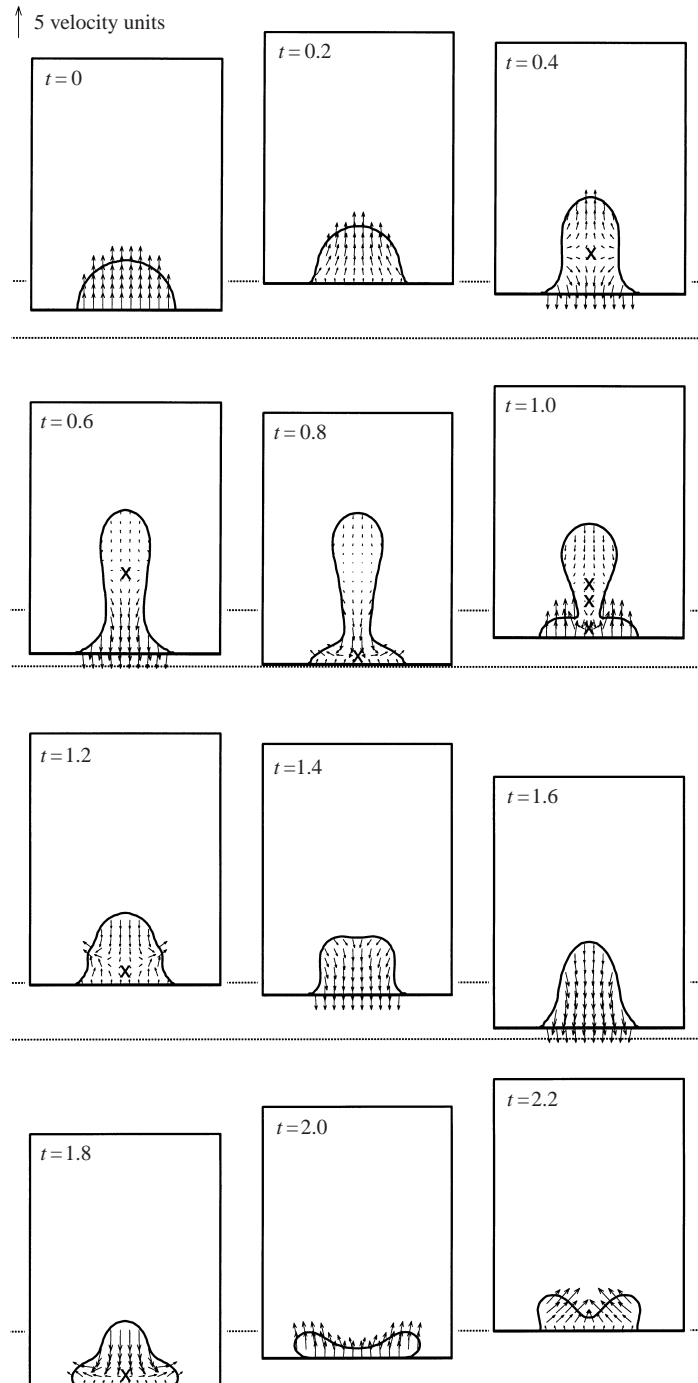


FIGURE 9. For caption see facing page.

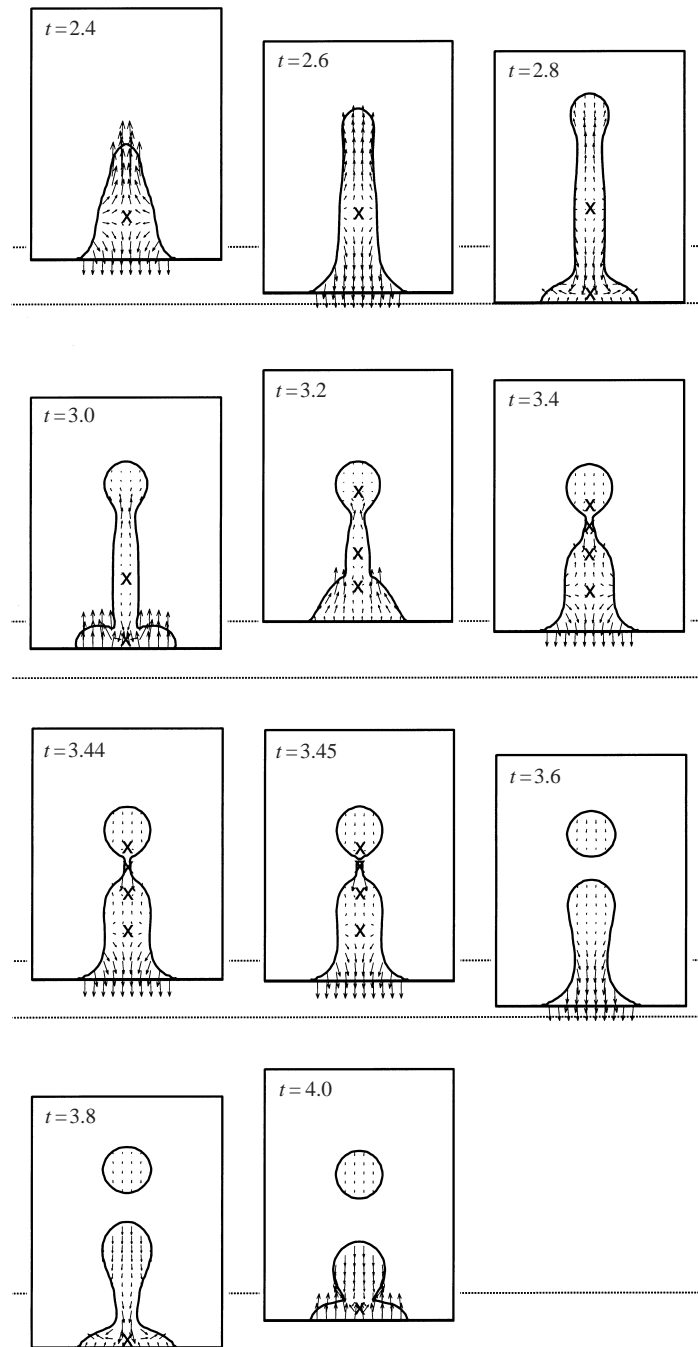


FIGURE 9. The droplet ejection process with the formation of a crater. Time is in periods. Velocity vectors are shown in every third cell. The horizontal lines indicate the minimum and maximum displacement of the base. Stagnation points are indicated by  $\times$ .  $Re = 10$ ,  $Bo = 0$ ,  $A = 18$ ,  $\Omega = 1$ ,  $\theta = 0$ ,  $\alpha = 0.001$ , and  $\beta = 0.001$ .  $30 \times 80$  grid cells in half of the domain shown.

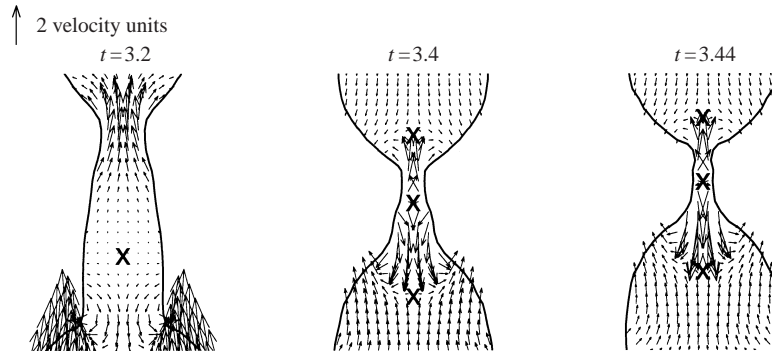


FIGURE 10. Close-up of pinch-off. Time is in periods. Velocity vectors are shown in every cell. Stagnation points are indicated by  $\times$ .  $Re = 10$ ,  $Bo = 0$ ,  $A = 18$ ,  $\Omega = 1$ ,  $\theta = 0$ ,  $\alpha = 0.001$ , and  $\beta = 0.001$ .  $30 \times 80$  grid cells.

the interface produce a negative pressure that causes flow toward the centre. Liquid approaching the axis cannot flow down into the base, so it flows upward, creating a spike with high inertia. This portion of the drop moves upward and the base moves downward (until  $t = 2.75$ ) and so the drop quickly becomes very elongated.

After this point the motion regains its similarity to the previous case. The dynamics between  $t = 2.75$  and ejection are similar to the dynamics between  $t = 0.75$  and ejection in the previous case. A neck forms and the uppermost portion of the drop becomes spherical. After a second stagnation point forms at the bottom, the lower portion of the drop widens. A third stagnation point forms in the upper portion when the tip of the drop reverses direction, then a fourth stagnation point forms when the base reverses direction at  $t = 3.25$ . Ejection occurs between  $t = 3.25$  and  $t = 3.5$ . Interestingly, ejection occurs in the same part of the cycle in these two cases and is exactly two cycles later in this second case. Unlike the previous case, the ejected droplet has downward momentum and eventually falls back into the lower portion of liquid.

In both cases the liquid remaining attached to the base after ejection continues to oscillate. In each case a crater forms, but the upward momentum of the resulting spike is insufficient for another droplet to be ejected.

In summary, when the forcing amplitude is high the initial inertia of the drop leads to the formation of a liquid spike that ejects a droplet. When the forcing amplitude is smaller this inertia is insufficient and the spike impacts the base to form a crater. The collapse of the crater leads to the formation of a second spike with enough inertia for droplet ejection to occur. When the amplitude is even smaller the inertia of the spike is not enough to lead to ejection. For the smallest forcing amplitudes a crater and spike do not form.

In some cases, when the forcing amplitude has an intermediate value, a crater may form and collapse to enclose a bubble. This is illustrated in figure 12 for  $A = 20$ . A segment of the time sequence is shown in which the crater collapses and a bubble is formed. Bubble entrapment happens when the rim of the crater collapses more quickly than the bottom of the crater. As the liquid rim closes over the bubble and approaches the axis of symmetry its radial momentum becomes vertical momentum. This momentum is directed both upward, to create a spike, and downward, into the bubble, thus deforming the bubble. The spike may or may not have sufficient inertia for droplet ejection to occur. In the numerical method compressibility is neglected.

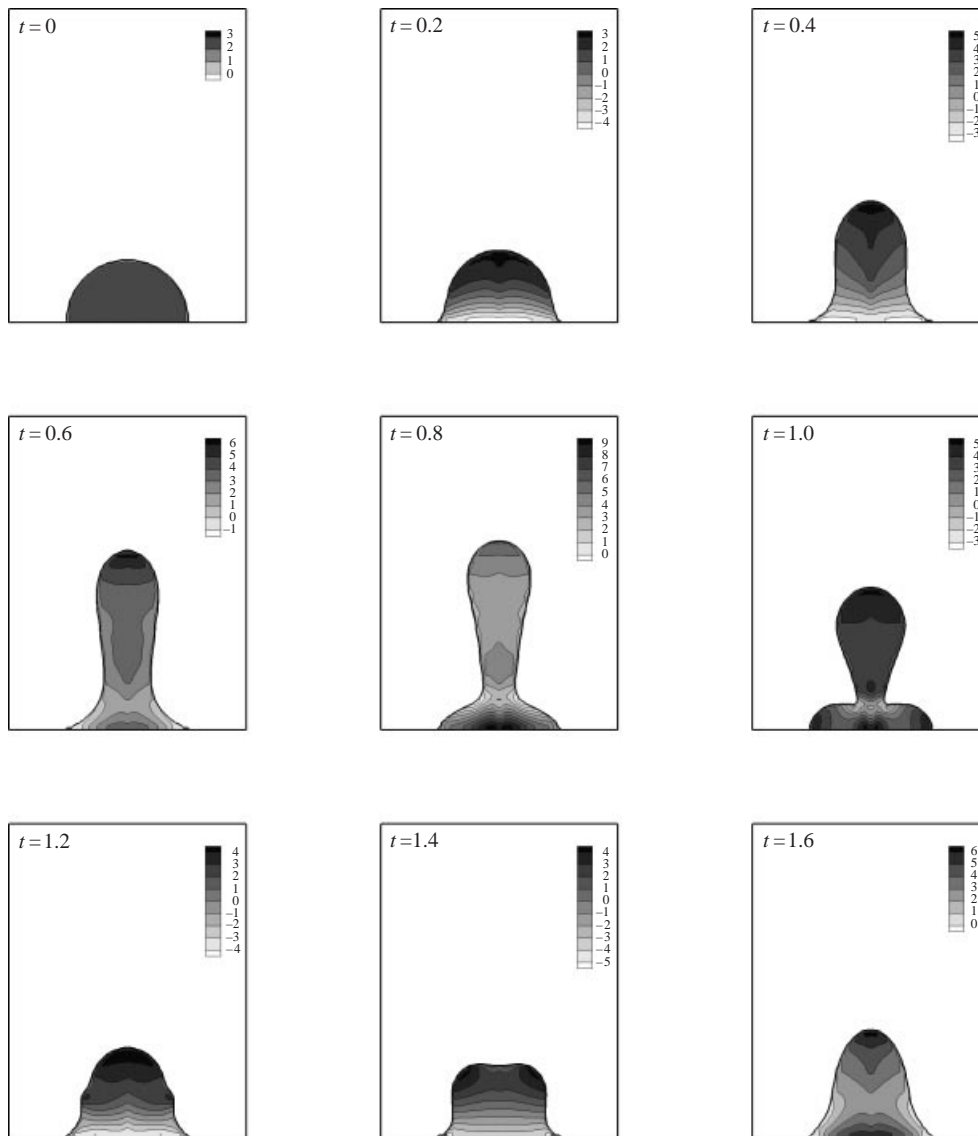


FIGURE 11. For caption see page 49.

Compressibility effects should be negligible except perhaps in the entrained bubble, where it would provide an additional mode of energy storage. Such energy transfer to the bubble could affect the process dynamics.

#### 4. Effect of parameter variations

The case presented in figures 6–8 was used as a basis from which the system parameters were varied in order to determine the effect of the parameters on the response. This effect was quantified via the volume of the ejected droplet, the velocity of the ejected droplet, and the time at which ejection occurred. Note that with the scaling used the ejected-droplet volume presented below is a fraction of the total liquid volume. The time of ejection is presented in units of forcing periods.

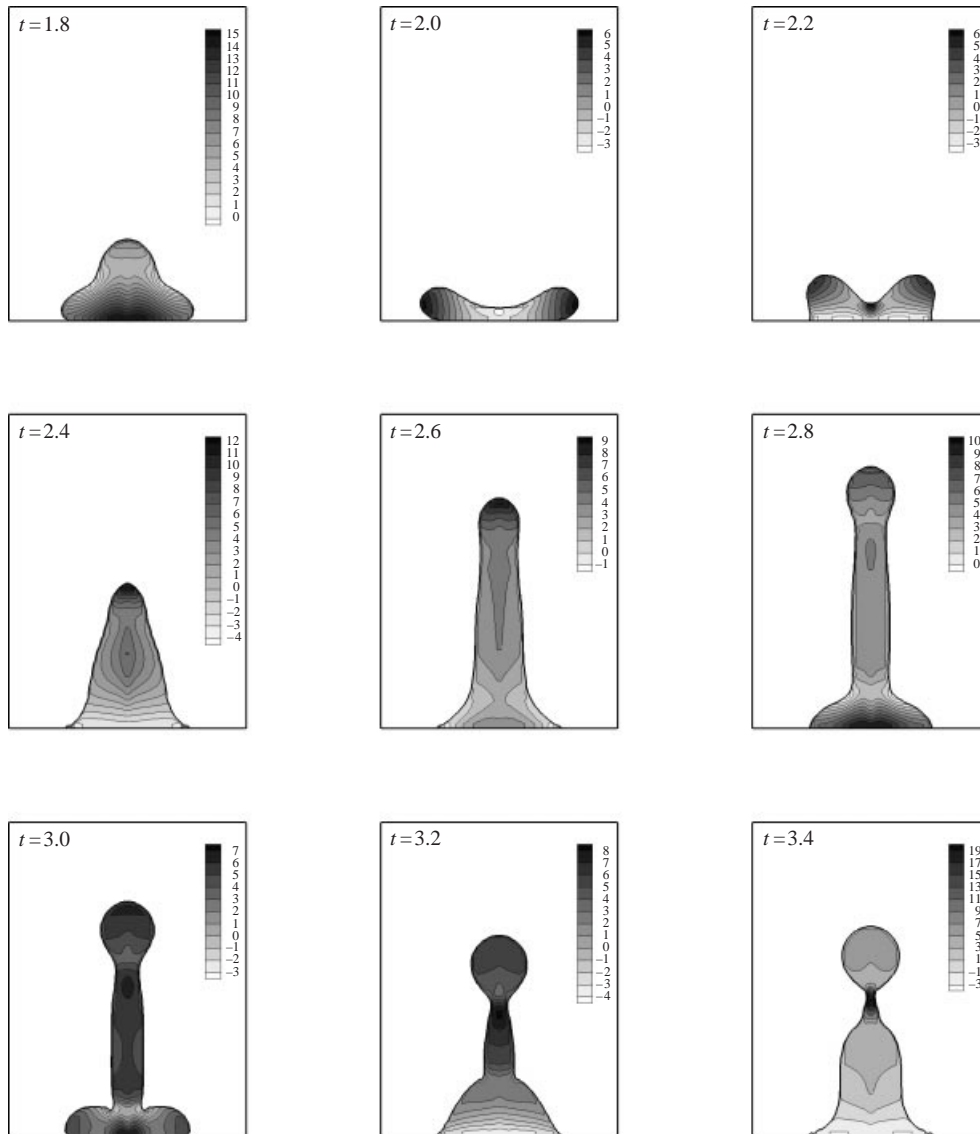


FIGURE 11. For caption see facing page.

The shape of the drop just prior to ejection was roughly the same for all parameter values. An example of this is in figure 9 at  $t = 3.2$ . The upper portion of the drop was approximately spherical, the central portion was cylindrical, and there was a wide region at the base. Although the shape of the drop was only qualitatively similar for other values of the parameters, this description of the drop shape is useful in understanding how changing the parameters alters the details of the ejection process. For different parameter values the relative sizes of the three regions are different. For example, the spherical region was significantly larger for the larger forcing amplitude in the case of figure 6 (see  $t = 1.2$ ). In both of those cases the cylindrical neck disappeared by the time of pinch-off, as the lower region became larger. In other cases the neck became very elongated and pinch-

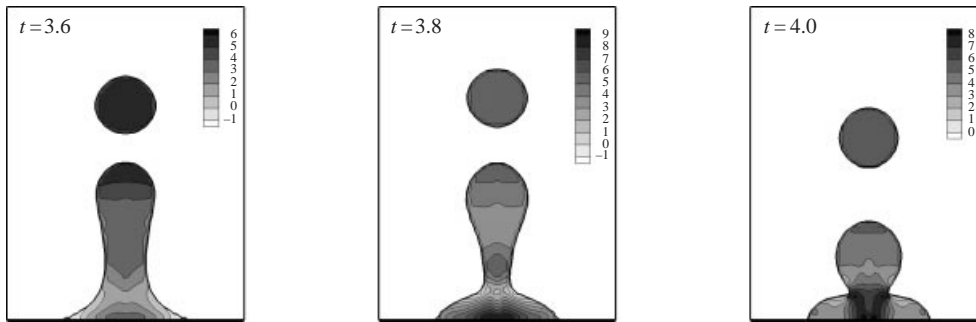


FIGURE 11. Pressure contours in the droplet ejection process with the formation of a crater. Time is in periods.  $Re = 10$ ,  $Bo = 0$ ,  $A = 18$ ,  $\Omega = 1$ ,  $\theta = 0$ ,  $\alpha = 0.001$ , and  $\beta = 0.001$ .  $30 \times 80$  grid cells in half of domain shown.

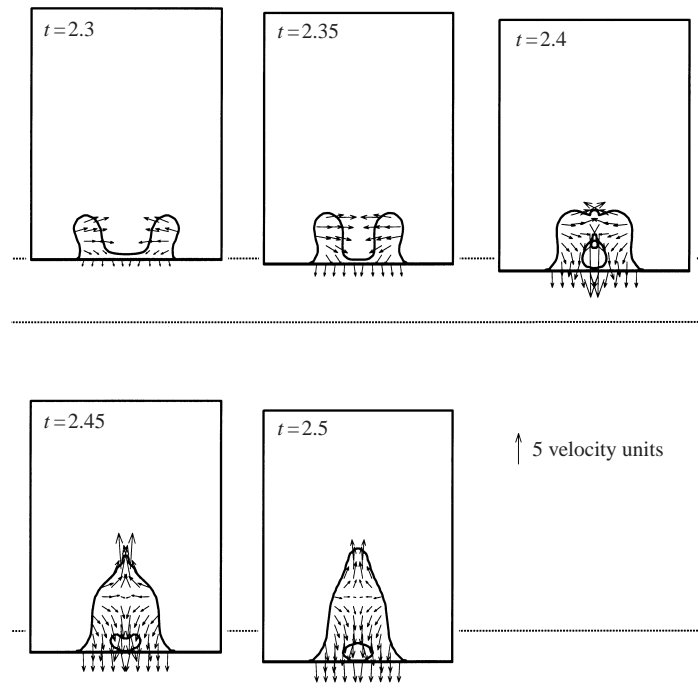


FIGURE 12. The bubble entrapment process. Time is in periods. Velocity vectors are shown in every third cell. The horizontal lines indicate the minimum and maximum displacement of the base.  $Re = 10$ ,  $Bo = 0$ ,  $A = 20$ ,  $\Omega = 1$ ,  $\theta = 0$ ,  $\alpha = 0.001$ , and  $\beta = 0.001$ .  $30 \times 80$  grid cells in half of domain shown.

off could occur at either the bottom or the top of the cylindrical region. When pinch-off occurred at the bottom the cylindrical region recoiled into the spherical region to form the secondary droplet. When pinch-off occurred at the top the cylindrical region recoiled towards the base and the spherical region alone constituted the secondary droplet. Under some conditions pinch-off occurred at both locations to form a satellite droplet, but only the first pinch-off event is considered in the present work. These findings are in qualitative agreement with those of Wilkes & Basaran (2001), but the results presented in this section go beyond what they present.

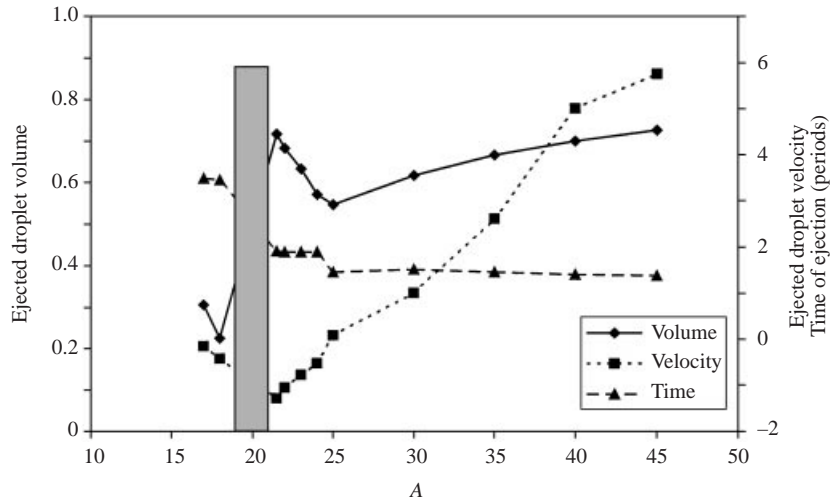


FIGURE 13. The effect of the forcing amplitude on the response.  $Re = 10$ ,  $Bo = 0$ ,  $\Omega = 1$ ,  $\theta = 0$ ,  $\alpha = 0.001$ , and  $\beta = 0.001$ . Ejection does not occur in the amplitude range delineated by the grey bar.

Figure 13 shows the effect of the forcing amplitude on ejection. Recall that this is the amplitude of the base acceleration, not of the base displacement. For low values of the forcing amplitude ejection did not occur, but a crater formed in the centre of the drop. As the forcing amplitude increased, the crater wall became steeper. For  $A = 16$ , a case in which ejection did not occur, the crater wall was at an angle of  $22^\circ$  with the horizontal when the drop radius reached a maximum. After this time the drop rebounded towards the centre. The angle later reached a maximum value of  $28^\circ$  as the crater was collapsing. Since the crater angle was small the resulting spike did not have enough energy for droplet ejection to occur. For the amplitude range  $17 \leq A \leq 18$ , ejection occurred from a spike that was produced by a crater. For  $A = 18$  the crater angle was  $34^\circ$  when the drop radius was maximized and it reached a maximum of  $46^\circ$ .

For  $19 \leq A \leq 21$ , ejection did not occur. A crater formed, but it collapsed to enclose a bubble. As the crater collapsed the liquid had large inward radial momentum. As the liquid approached the centreline this was transferred to vertical momentum. When the crater collapsed along the base, as for  $17 \leq A \leq 18$ , all this momentum was upward. However in this amplitude range, the rim of the crater collapsed to enclose a bubble, so the radial momentum was transferred into both upward momentum (which led to the formation of a spike) and downward momentum (into the bubble). Therefore, although a spike was formed it did not have as much inertia, so ejection did not occur. For  $A = 20$  the crater angle was  $46^\circ$  when the drop radius was maximized. The angle was  $112^\circ$  just before the rim of the crater reached the centre to enclose a bubble. In their study of crater collapse, Zeff *et al.* (2000) also found that a high-momentum spike was not created when a bubble was enclosed.

When the amplitude was increased to above  $A = 21$ , ejection occurred without the formation of a crater. This change in the type of ejection caused a sharp increase in the droplet volume and a decrease in the time of ejection. Increasing the amplitude from this point caused the ejected-droplet volume to decrease and the ejected-drop velocity to increase, while the ejection time remained fairly constant. The neck formed

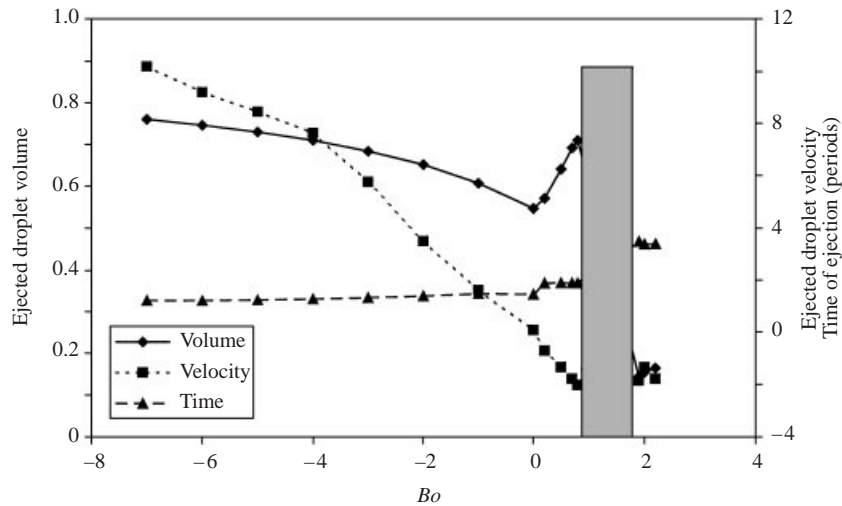


FIGURE 14. The effect of the Bond number on the response.  $Re = 10$ ,  $A = 25$ ,  $\Omega = 1$ ,  $\theta = 0$ ,  $\alpha = 0.001$ , and  $\beta = 0.001$ . Ejection does not occur in the amplitude range delineated by the grey bar.

in the first forcing cycle thinned until the upward motion of the base caused it to be filled. Subsequent downward motion of the base in the second cycle caused the neck to thin once again, and pinch off. At approximately  $A = 25$  a transition occurred. Above the transition the neck did not fill and re-thin during the second cycle, but thinned continuously. Therefore ejection occurred sooner and at the transition amplitude there was a decrease in the ejection time. Above the transition amplitude the ejection time remained constant and the ejected-droplet volume and velocity increased. Increasing the amplitude caused the primary drop to become more elongated, particularly the central cylindrical region. This region pinched off at the bottom, so as it became bigger the secondary droplet became bigger.

Next, the effect of the Bond number is considered. Recall that gravity acts downward when the Bond number is positive. As a point of reference, the Bond number was 1.30 for experiments in normal gravity, using a  $30\ \mu\text{l}$  water drop. As shown in figure 14, the ejected-droplet volume and velocity decreased, and the ejection time weakly increased, as the Bond number increased from  $Bo = -7$  to 0. This is simply because an upward gravitational force aids ejection. As  $Bo$  increased, the length of the cylindrical portion of the drop decreased, so the secondary droplet volume decreased since the drop pinched off near the bottom. Between Bond numbers of 0 and about 0.8 the upward motion of the base caused the neck to fill before it could break, so ejection occurred slightly later. Additionally, the ejected-droplet volume increased as the Bond number increased in this range. For the highest Bond numbers on these curves,  $Bo \geq 1.9$ , droplet ejection occurred after a crater and a spike had formed. There was no crater in the other Bond number cases. This accounts for the large difference between the droplet volume and ejection time of the highest Bond number case compared to the other cases. Ejection did not occur for Bond numbers greater than 2. Additionally, ejection did not occur for  $0.9 \leq Bo \leq 1.8$ . Instead, a crater formed and collapsed to enclose a bubble. A spike formed, but it did not have enough inertia to lead to ejection. Notice that this graph is qualitatively a mirror image of figure 13. Increasing the forcing amplitude and decreasing gravity have the same effect on the process.

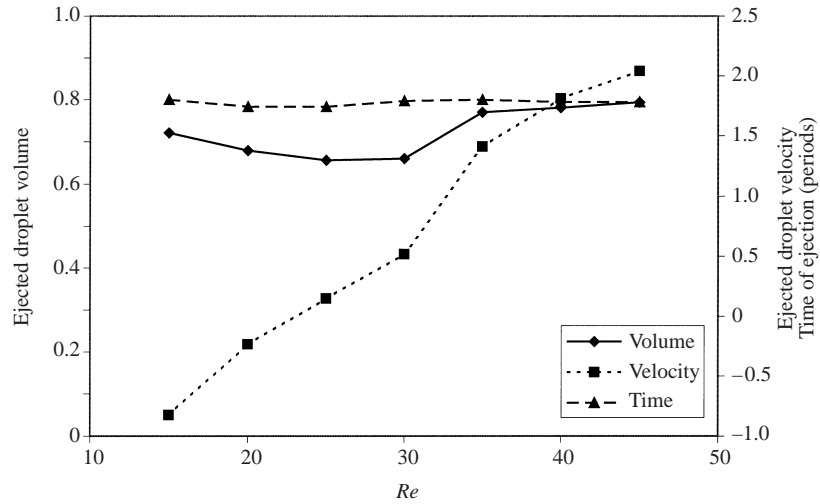


FIGURE 15. The effect of the Reynolds number on the response.  $Bo = 0$ ,  $A = 20$ ,  $\Omega = 1$ ,  $\theta = 0$ ,  $\alpha = 0.001$ , and  $\beta = 0.001$ .

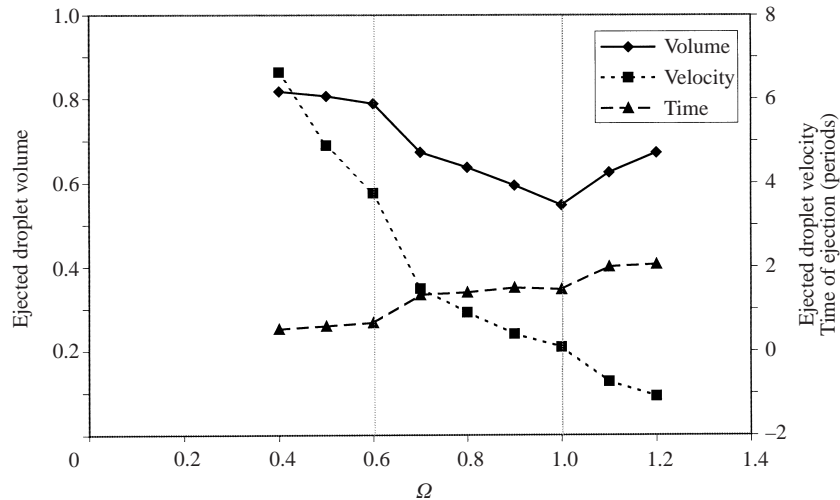


FIGURE 16. The effect of the forcing frequency on the response. The vertical lines indicate transition points.  $Re = 10$ ,  $Bo = 0$ ,  $A = 25$ ,  $\theta = 0$ ,  $\alpha = 0.001$ , and  $\beta = 0.001$ .

The effect of the Reynolds number on the response is shown in figure 15. When the Reynolds number was low, viscous forces inhibited droplet ejection. When the Reynolds number was high, parasitic errors due to the CSF method were not sufficiently damped and the computation failed. There was a jump in the ejected-droplet volume and velocity as the Reynolds number was increased from 30 to 35. This jump occurred because the secondary droplet pinched off at the top of the central cylindrical region when the Reynolds number was low and at the bottom when the Reynolds number was high. Otherwise, the Reynolds number affected the ejected-droplet volume and the time of ejection only weakly. The ejected-droplet velocity increased as the Reynolds number increased because the damping decreased.

The effect of the forcing frequency on ejection is shown in figure 16. Although the acceleration amplitude of the base was fixed, the velocity amplitude and the

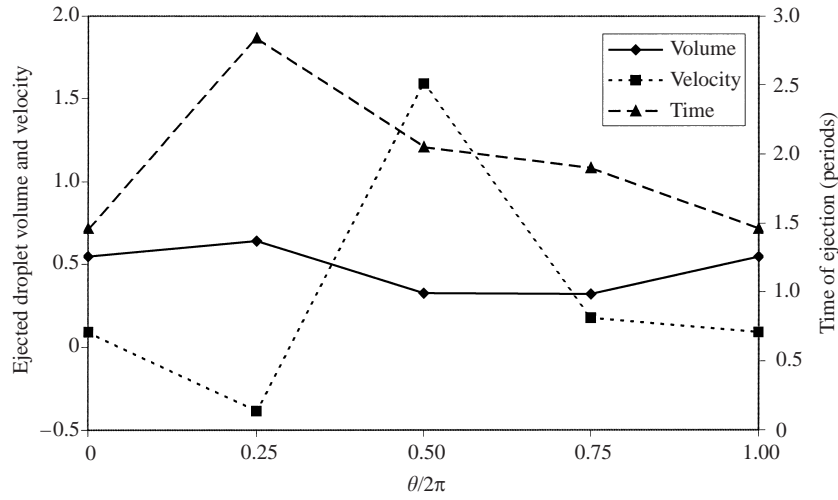


FIGURE 17. The effect of the phase of the base oscillations on droplet ejection.  $Re = 10$ ,  $Bo = 0$ ,  $A = 25$ ,  $\Omega = 1$ ,  $\alpha = 0.001$ , and  $\beta = 0.001$ .

displacement amplitude of the base decreased as the forcing frequency increased. When the forcing frequency was small the primary drop became very elongated, ejection occurred during the first cycle, pinch-off was near the base of the drop, and the ejected-droplet velocity was large. As the forcing frequency was increased, the elongation of the drop decreased and so the ejected-droplet volume and velocity decreased and the ejection time increased slightly. Above  $\Omega = 0.6$  the initial inertia of the drop was not sufficient for ejection to occur during the first forcing cycle. This led to a jump in the ejection time. Since ejection occurred later, the drop inertia had time to decrease, so there was a sharp decrease in the ejected-droplet velocity. There was also a decrease in the ejected-droplet volume because the main drop was not as elongated. As the frequency was increased from this point the volume and velocity continued to decrease and the ejection time continued to increase. Like lowest frequencies, the elongation of the drop, particularly the central cylindrical portion, decreased as the frequency increased, leading to the decrease in ejected-droplet volume. This trend continued until the cylindrical region disappeared at  $\Omega = 1$ . Above this frequency the central cylindrical region filled before ejection could occur, but another cylindrical neck formed later in the cycle. A secondary droplet then pinched off from the top of the neck. Because of this there was another jump in the ejection time and a corresponding drop in the ejection velocity. For  $\Omega > 1$ , as for lower frequencies, the elongation of the second cylindrical region decreased as the frequency increased. However, more liquid flowed into the upper spherical portion of the drop than for the lower frequencies, leading to a larger ejected-droplet volume. Above  $\Omega = 1.2$  this second neck disappeared and ejection did not occur. For  $\Omega = 1.3$  a crater formed in the fourth forcing cycle, but it collapsed to enclose a bubble and ejection did not occur.

The initial phase of the forcing had a substantial effect on ejection as illustrated in figure 17. The dynamics when  $\theta = 0$  were discussed in the previous section. A phase of  $\theta = 2\pi$  is equivalent. The dynamics for three other values of the phase are discussed now.

When the phase was  $\pi/2$  the motion began with the base at its maximum displacement. The initial velocity was zero, so the drop had no inertia. As the base moved

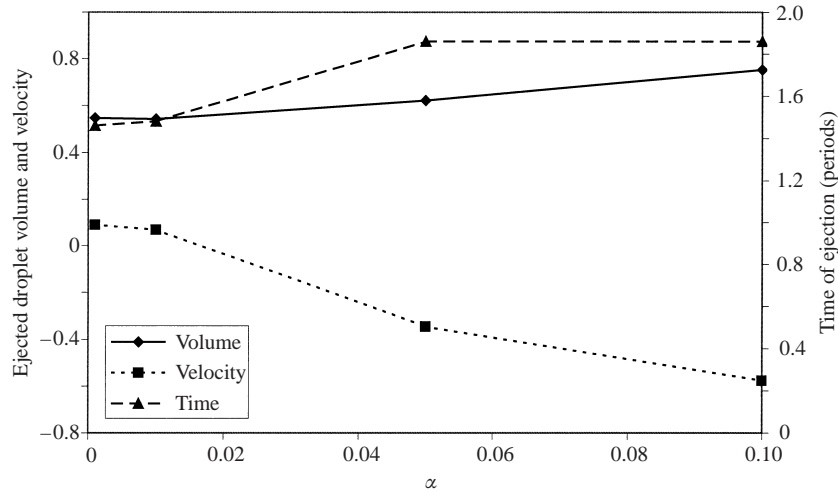


FIGURE 18. The effect of the density ratio on the response.  $Re = 10$ ,  $Bo = 0$ ,  $A = 25$ ,  $\Omega = 1$ ,  $\theta = 0$ , and  $\beta = 0.001$ .

down it pulled the drop down and imparted downward momentum to it. Then as the base moved upward this downward momentum was transferred into outward radial momentum. The drop flattened and a crater formed. Then as the base moved down again the crater collapsed to enclose a bubble and create a spike. Eventually, a secondary droplet pinched off the end of the spike. The ejected-droplet velocity was negative, so it quickly fell back into the primary drop.

When the initial phase was  $\pi$  the computation started with the base at its midpoint and initially moving downward, so the drop had downward inertia. When it then started moving upward the downward momentum of the drop became radial momentum and a crater formed. The crater then collapsed, without enclosing a bubble, to create a spike with even greater momentum than in the  $\theta = \pi/2$  case, so the secondary droplet that subsequently formed had a larger velocity.

Finally, when the initial phase was  $3\pi/2$  the simulation began with the base at its minimum location. The drop had no inertia. As the base moved up the drop flattened and gained upward momentum. Then as the base moved down the drop became elongated. The base then moved upward again and the upper portion of the drop filled to become more spherical. A droplet pinched off during the next stage as the base moved downward.

Of these values of the phase,  $\pi$  is the optimum because the ejected-droplet velocity is maximized. A crater will always form for this value of the phase, unless the forcing amplitude is very small. The collapse of the crater will then lead to the formation of a liquid spike with high momentum. Therefore, using this phase is an effective way to ensure that the momentum of the liquid spike is high. Because of this, droplet ejection can be achieved with a lower forcing amplitude.

The effect of the density and viscosity ratios on ejection is given in figures 18 and 19, respectively. Recall that the density ratio is the density of the gas surrounding the drop divided by the density of the drop. Likewise, the viscosity ratio is the viscosity of the gas surrounding the drop divided by the viscosity of the drop. Increasing either the density ratio or the viscosity ratio causes the ejected-droplet volume to increase, the ejected-droplet velocity to decrease, and the time of ejection to increase. When the density ratio was increased, the density, and hence the inertia, of the medium

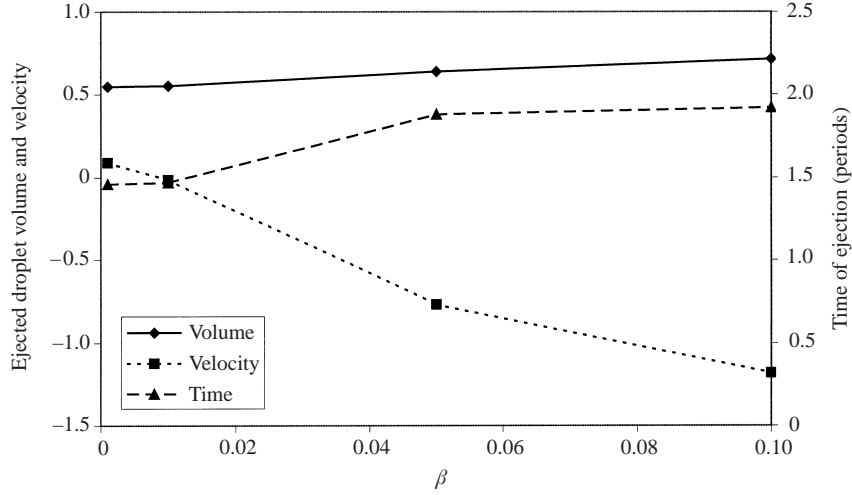


FIGURE 19. The effect of the viscosity ratio on the response.  $Re = 10$ ,  $Bo = 0$ ,  $A = 25$ ,  $\Omega = 1$ ,  $\theta = 0$ , and  $\alpha = 0.001$ .

surrounding the drop increased. Thus, the medium surrounding the drop offered more resistance to the motion of the drop. When the viscosity ratio was increased, the viscosity of the medium surrounding the drop increased. Thus, there was more viscous damping in the surrounding medium to resist the motion of the drop. This is why ejection occurred later and with lower velocity when either  $\alpha$  or  $\beta$  was increased. Also, the elongation of the drop decreased as either  $\alpha$  or  $\beta$  was increased. The effects of the other parameters showed that less elongation of the primary drop means that the central cylindrical region of the drop becomes shorter and the volume of the ejected droplet becomes smaller. The effect of the density and viscosity ratios is different. Although the tip of the drop is inhibited from moving upward, fluid moving upward within the neck of the drop is not inhibited. Therefore, the spherical region at the top of the drop is larger. In this way, increasing the density or viscosity ratio causes the ejected-droplet volume to increase.

## 5. Ejection threshold

The forcing amplitude above which droplet ejection occurs has been studied experimentally by Goodridge *et al.* (1996, 1997) and by Range *et al.* (2001). Range *et al.* consider ejection from a drop, while Goodridge *et al.* studied ejection from a layer. In both sets of experiments several liquids were used to determine the effect of the fluid properties on the ejection threshold.

In the experiments of Goodridge *et al.* the lateral extent of the layer was much larger than the capillary wavelengths excited, so edge effects were not important. This also led to a different scaling than is used in the present work, since no external length scale was important. They defined a dimensionless frequency,  $\omega^*$ , and a dimensionless amplitude,  $a^*$ , that are related to the present scaling and to the dimensional variables as follows:

$$\omega^* = \frac{\Omega}{Re^3} = \frac{\omega \mu_L^3}{\rho_L \sigma^2}, \quad (7)$$

$$a^* = \frac{A}{Re^4} = \frac{a \mu_L^4}{\rho_L \sigma^3}. \quad (8)$$

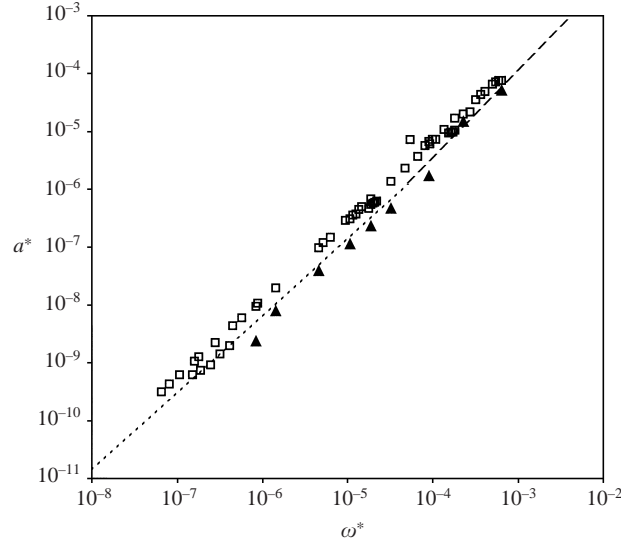


FIGURE 20. The droplet ejection threshold. Filled symbols: present simulations. Open symbols: experimental data of Range *et al.* Dotted line: low-viscosity correlation of Goodridge *et al.* Dashed line: high-viscosity correlation of Goodridge *et al.*

This viscous scaling may not be appropriate over the entire Reynolds number range considered, but it is convenient for comparison of the data. The threshold value of  $a^*$  above which ejection occurs was determined. The following correlations of the threshold of  $a^*$  as a function of  $\omega^*$  were determined for high- and low-viscosity fluids by Goodridge *et al.* (1997):

$$a^* = 0.261(2\omega^*)^{4/3} \quad \text{for low } \mu_L, \quad (9)$$

$$a^* = 1.306(2\omega^*)^{3/2} \quad \text{for high } \mu_L. \quad (10)$$

The response of a liquid layer to the forcing is subharmonic, whereas the response of a drop is harmonic. Because of this difference the correlations above have been modified by multiplying the forcing frequency by a factor of two. This makes them more directly comparable with the results of the present simulations, and of Range *et al.*, for the vibration of a drop.

Range *et al.* also found the threshold value of  $a^*$  as a function of  $\omega^*$ , but for ejection from a drop instead of from a layer. In that work, the capillary wavelength may be on the order of the drop diameter. They used more than one drop size in order to determine the effect of the size on the ejection threshold, but this parameter did not seem to affect the results.

Simulations were run to duplicate several of the experiments of Range *et al.* Their drop sizes, fluid properties, and driving frequencies were used to determine the values of the system parameters. The dimensionless driving amplitude was then varied to find the ejection threshold. The forcing amplitude was deemed to be below the threshold if ejection did not occur within five forcing periods and above the threshold if it did occur within five periods.

Figure 20 shows the droplet ejection threshold in terms of the variables  $a^*$  and  $\omega^*$ . The experimental data of Range *et al.*, the correlations of Goodridge *et al.*, and the results of the present simulations are shown. The threshold amplitude increases monotonically with frequency. The large range of  $\omega^*$  that is covered by the experiments

cannot all be simulated with the present method. At low values of  $\omega^*$  the viscosity is low, so parasitic errors are not damped and non-physical features of the interface grow in time. For this reason values of  $\omega^*$  less than about  $10^{-6}$  were not considered. At high values of  $\omega^*$ , annular regions of liquid break off from the outer edge of the primary drop in the simulations. Such behaviour is clearly unstable to azimuthal modes that cannot be captured in these axisymmetric simulations. The highest two values of  $\omega^*$  considered are in this regime, so the relevance and accuracy of these points are uncertain.

In general, the computed threshold points are lower than the threshold correlations of Goodridge *et al.*, which are lower than the data of Range *et al.* The main difference between the present computations and the experiments of Range *et al.* is the initial conditions. In the computations, the forcing was applied as a step function, whereas it was ramped up in the experiments. It was not practical to ramp up the forcing in the computations for two reasons. First, the simulations required a substantial amount of time to run. All the simulations were limited to five forcing cycles, at most, to ensure that a reasonable number of cases could be completed. Second, parasitic errors grew as the computation progressed and eventually became unacceptably large. Limiting the computations to five forcing cycles ensured that the parasitic errors were small in most of the cases considered. The difference in the initial conditions most probably accounts for the difference between the threshold of the present computations and the threshold of the experiments of Range *et al.* Since the forcing was stepped in the numerical simulations and ejection occurred within the first five cycles the system had not yet attained periodic motion. Thus, transient overshoot was present in the response of the simulations and could most likely account for the differences that are seen.

The initial conditions of the experiments of Range *et al.* and the experiments of Goodridge *et al.* were more closely comparable since the forcing was ramped in both cases. However, they were not the same. Goodridge *et al.* first set the forcing amplitude high enough that ejection occurred and then decreased it slowly until ejection stopped. This approach was feasible because the depth of the layer was unimportant. Therefore, it did not matter if some of the ejected droplets did not fall back into the liquid layer. Range *et al.* found the ejection threshold by increasing the forcing amplitude slowly until droplet ejection was observed.

A much more important difference in the two sets of experiments was the liquid configuration. The curvature of the interface of the liquid drop influenced the response, and the capillary wavelength that was excited was on the order of the drop size. Also, the contact line was pinned in the drop experiments of Range *et al.* These edge effects tend to stabilize the system by limiting the available wave modes. This is why the threshold of Range *et al.* is above that of Goodridge *et al.*

Regardless of the differences, figure 20 shows that the two sets of experiments and the present computations result in the same basic trend for the ejection threshold. The experimental data of Range *et al.* are greater than the correlations of Goodridge *et al.* by a factor of 1.5 on average. The results of the simulations are less than the correlations by an average factor of 1.4. To further quantify the comparison, curve fits in the form of equations (9) and (10) were computed for the simulation results and for the data of Range *et al.* In the low-frequency regime, the exponent was 1.40 for the simulations and 1.37 for the data of Range *et al.* These values compare well with the exponent of 1.33 in the correlation of Goodridge *et al.* In the high-frequency regime, the exponent was 1.74 for the simulations, 1.27 for the data of Range *et al.* and 1.50 in the correlation of Goodridge *et al.* However, only three simulations were performed

in this regime. One of these is very near the transition from low to high frequency, and the accuracy of the other two is questionable, as mentioned above, so the accuracy of the power-law exponent is uncertain.

## 6. Conclusion

The forcing frequency has a great effect on the response of a liquid drop to vertical, oscillatory forcing. When the frequency is low, the motion is axisymmetric. Only low-order modes are excited. When droplet ejection occurs, a single secondary droplet pinches-off from a spike or wave crest at the centre of the drop. When the forcing frequency is high, high-order, azimuthal modes are excited and the free-surface response is very chaotic. When droplet ejection occurs, numerous secondary droplets are ejected simultaneously from the entire surface of the primary drop to create a spray of fairly uniform droplets. Sprays of this kind may be used in many applications, several of which are the subject of current research. This type of forcing may also be used for applications that do not involve a spray, such as emulsification.

Interestingly, although the response appears to be quite different in the low- and high-frequency regimes, there is an important similarity. In both cases a crater may form on the free surface of the drop. When the crater collapses a liquid spike with large, upward momentum is created. Droplet ejection occurs when a droplet pinches off from the end of the spike. In the low-frequency regime, the crater and spike always occur in the centre and they dominate the evolution of the entire drop. In the high-frequency regime, waves occur at multiple locations on the surface of the drop simultaneously. A crater may form at a single wave site, at just a few wave sites, or at many of them, depending on the forcing conditions. Thus, crater formation is a local event and can occur anywhere on the drop free surface. It does not seem to affect the motion of the rest of the drop. Because the cratering aspect of the droplet-ejection phenomenon occurs at all frequencies, parallels can be drawn between the low- and high-frequency regimes.

In this paper, low-frequency droplet ejection was studied using numerical simulations. The transient, axisymmetric governing equations were solved using a finite-volume projection method. A qualitative comparison between the computed shape of the interface (figure 2) and related experimental images (figure 1) for ejection from a 30  $\mu\text{l}$  water drop being vibrated at 61 Hz with an amplitude of  $66 \text{ m s}^{-2}$  showed that the numerical method is able to display realistic flow dynamics. In the remainder of the computations the Reynolds number was smaller to minimize parasitic errors. The forcing amplitude was correspondingly higher. In the majority of the simulations the Bond number was zero and the dimensionless forcing frequency 1.

The details of the flow fields of two cases, one in which ejection occurred after a crater had been formed and one without a crater, were studied. The only difference between the two cases was the forcing amplitude. During the second forcing period, ejection occurred from a liquid spike for the high-amplitude case, but the spike in the low-amplitude case did not have sufficient inertia to cause ejection. After this point the crater formed in the low-amplitude case. The crater collapsed to form a smaller diameter spike, but one that had greater inertia than the initial spike, so ejection occurred. The dynamics of the two cases were very similar near the time of ejection. Ejection occurred later for the case with a crater, but at the same phase of the forcing cycle.

The effect of the physical parameters on droplet ejection was quantified via the volume of the ejected droplet, the velocity of the ejected droplet, and the time at

which ejection occurred. Increasing the forcing amplitude caused the volume and velocity to increase and the ejection time to slightly decrease. Increasing the Bond number (increasing gravity) had the opposite effect. Increasing the Reynolds number caused the velocity to increase considerably, but affected the volume and ejection time only weakly. Increasing the forcing frequency, while holding the amplitude constant, caused the ejected-droplet volume and velocity to decrease and the ejection time to increase. If the velocity amplitude was held constant, increasing the forcing frequency caused the ejected-droplet velocity and the ejection time to increase, but did not effect the ejected-droplet volume. Setting the forcing phase to  $\pi$ , which is equivalent to beginning with the base located at its midpoint and moving downward, maximized the ejection velocity.

Vibration-induced droplet ejection is interesting because it is a novel method to form a spray, and may have many industrial applications. The low- and high-frequency regimes are related in that ejection occurs similarly in both cases, but the overall motion appears quite different. Only in the regime where a crater forms and collapses is the dynamics of droplet ejection similar in both cases. Further study is warranted because both regimes contain interesting and important problems with rich dynamics.

Investigation of various aspects of the vibration-induced flow is continuing, including the following components. The effect of contact line motion on the ejection dynamics will be studied. It is of particular interest that the crater formation is significantly altered if the contact line is permitted to move. Three-dimensional computations will be performed, in a frequency range in which azimuthal wave modes are excited, to examine the coupling of wave modes and the effect of azimuthal motion on ejection. The formation of satellite droplets will be investigated. Ejection from a liquid layer will be simulated to evaluate the effect of the free-surface configuration on the ejection process. Additionally, the relationship between vibration-induced droplet ejection, bubble entrapment, and the Rayleigh–Taylor instability will be analysed.

This work was supported by the NASA Microgravity Research Division under contract NAG3-1945 and the Hoechst Celanese Corporation. The experimental contributions of Kai Range and Bojan Vukasinovic are greatly appreciated. The authors are grateful to the referees for their valuable suggestions. Additionally, we would like to thank Ed Wilkes and Osman Basaran for providing us with their data.

#### REFERENCES

- BASARAN, O. A. & DEPAOLI, D. W. 1994 Nonlinear oscillations of pendant drops. *Phys. Fluids* **6**, 2923–2943.
- BENJAMIN, T. B. & URSELL, F. 1954 The stability of the plane free surface of a liquid in vertical periodic motion. *Proc. R. Soc. Lond. A* **225**, 505–515.
- BERIS, A. N., RICHARDS, J. R. & LENHOFF, A. M. 1996 A volume of fluid method applied to liquid–liquid jet breakup and drop dynamics. In *Advances in Multi-fluid Flows* (ed. Renardy, Coward, Papageorgiou & Sun), pp. 349–367.
- BESSION, T., EDWARDS, W. S. & TUCKERMAN, L. S. 1996 Two-frequency parametric excitation of surface waves. *Phys. Rev. E* **54**, 507–513.
- BRACKBILL, J. U., KOTHE, D. B. & ZEMACH, C. 1992 A continuum method for modeling surface tension. *J. Comput. Phys.* **100**, 335–354.
- CHEN, A. U. & BASARAN, O. A. 2002 A new method for significantly reducing drop radius without reducing nozzle radius in drop-on-demand drop production. *Phys Fluids* **14**, L1–L4.
- CHIBA, M. & WAKAMATSU, J. 1997 Hydroelastic coupled vibration of a liquid drop attached to a thin walled structure in a low-gravity condition, Part II, Static and dynamic behavior of a liquid drop on earth. *J. Japan Soc. Microgravity Appl.* **14**, 29–30.

- CILIBERTO, S., DOUADY, S. & FAUVE, S. 1991 Investigating space-time chaos in Faraday instability by means of the fluctuations of the driving acceleration. *Europhys. Lett.* **15**, 23–28.
- CILIBERTO, S. & GOLLUB, J. P. 1984 Pattern competition leads to chaos. *Phys. Rev. Lett.* **52**, 922–925.
- CILIBERTO, S. & GOLLUB, J. P. 1985 Chaotic mode competition in parametrically forced surface waves. *J. Fluid Mech.* **158**, 381–398.
- COWARD, A. V., RENARDY, Y. Y., RENARDY, M. & RICHARDS, J. R. 1997 Temporal evolution of periodic disturbances in two-layer Couette flow. *J. Comput. Phys.* **132**, 346–361.
- DECENT, S. P. & CRAIK, D. D. 1995 Hysteresis in Faraday resonance. *J. Fluid Mech.* **293**, 237–268.
- DEPAOLI, D. W., SCOTT, T. C. & BASARAN, O. A. 1992 Oscillation frequencies of droplets held pendant on a nozzle. *Separation Sci. Tech.* **27**, 2071–2082.
- EDWARDS, W. S. & FAUVE, S. 1994 Patterns and quasi-patterns in the Faraday experiment. *J. Fluid Mech.* **278**, 123–148.
- EGGERS, J. 1997 Nonlinear dynamics and breakup of free-surface flows. *Rev. Mod. Phys.* **69**, 865–929.
- FARADAY, M. 1831 On the forms and states assumed by fluids in contact with vibrating elastic surfaces. *Phil. Trans. R. Soc. Lond.* **52**, 319–340.
- FROHN, A. & ROTH, N. 2000 *Dynamics of Droplets*. Springer.
- FUKAI, J., SHIIBA, Y., YAMAMOTO, T., MIYATAKE, O., POULIKAKOS, D., MEGARIDIS, C. M. & ZHAO, Z. 1995 Wetting effects on the spreading of a liquid droplet colliding with a flat surface: experiment and model. *Phys. Fluids* **7**, 236–247.
- FUKAI, J., ZHAO, Z., POULIKAKOS, D., MEGARIDIS, C. M. & MIYATAKE, O. 1993 Modeling of the deformation of a liquid droplet impinging upon a flat surface. *Phys. Fluids A* **5**, 2588–2599.
- GAÑÁN, A. & BARRERO, A. 1990 Free oscillations of liquid captive drops. *Microgravity Sci. Technol.* **III**, **2**, 70–86.
- GIAVEDONI, M. D. 1995 A numerical study of the two-dimensional dynamic behavior of a thin liquid film subject to a vertical oscillation. *Ind. Engng Chem. Res.* **34**, 356–365.
- GOLUB, G. H. & VAN LOAN, C. F. 1989 *Matrix Computations*. The Johns Hopkins University Press.
- GOODRIDGE, C. L., SHI, W. T., HENTSCHEL, H. G. E. & LATHROP, D. P. 1997 Viscous effects in droplet-ejecting capillary waves. *Phys. Rev. E* **56**, 472–475.
- GOODRIDGE, C. L., SHI, W. T. & LATHROP, D. P. 1996 Threshold dynamics of singular gravity-capillary waves. *Phys. Rev. Lett.* **76**, 1824–1827.
- GUEYFFIER, D., LI, J., NADIM, A., SCARDOVELLI, R. & ZALESKI, S. 1999 Volume-of-fluid interface tracking with smoothed surface stress methods for three-dimensional flows. *J. Comput. Phys.* **152**, 423–456.
- HARLOW, F. H. & WELCH, J. E. 1965 Numerical calculation of time-dependent viscous incompressible flow of fluid with free surface. *Phys. Fluids* **8**, 2182–2189.
- HIRT, C. W. & NICHOLS, B. D. 1981 Volume of fluid (VOF) method for the dynamics of free boundaries. *J. Comput. Phys.* **39**, 201–225.
- HOGREFE, J. E., PEFFLEY, N. L., GOODRIDGE, C. L., SHI, W. T., HENTSCHEL, H. G. E. & LATHROP, D. P. 1998 Power-law singularities in gravity-capillary waves. *Physica D* **123**, 183–205.
- JAMES, A. J. 2000 Vibration induced droplet ejection. PhD thesis, Georgia Institute of Technology.
- JAMES, A. J., VUKASINOVIC, B., SMITH, M. K. & GLEZER, A. 2003 Vibration-induced drop atomization and bursting. *J. Fluid Mech.* **476**, 1–28.
- JIANG, L., TING, C.-L., PERLIN, M. & SCHULTZ, W. W. 1996 Moderate and steep Faraday waves: instabilities, modulation and temporal asymmetries. *J. Fluid Mech.* **329**, 275–307.
- KERSHAW, D. S. 1978 The incomplete Cholesky-conjugate gradient method for the iterative solution of systems of linear equations. *J. Comput. Phys.* **26**, 43–65.
- KOTHE, D. B., MJOLSNESS, R. C. & TORREY, M. D. 1991 RIPPLE: A computer program for incompressible flows with free surfaces. *Los Alamos National Lab Rep.* LA-12007-MS.
- KOTHE, D. B., RIDER, W. J., MOSSO, S. J., BROCK, J. S. & HOCHSTEIN, J. I. 1996 Volume tracking of interfaces having surface tension in two and three dimensions. *AIAA Paper* 96-0859.
- KUMAR, K. 1996 Linear theory of Faraday instability in viscous liquids. *Proc. R. Soc. Lond. A* **452**, 1113–1126.
- KUMAR, K. & TUCKERMAN, L. S. 1994 Parametric instability of the interface between two fluids. *J. Fluid Mech.* **279**, 49–68.
- LI, J., RENARDY, Y. & RENARDY, M. 2000 Numerical simulations of breakup of a viscous drop in simple shear flow through a volume-of-fluid method. *Phys. Fluids* **12**, 269–282.

- LIUBASHEVSKI, O., FINEBERG, J. & TUCKERMAN, L. S. 1997 Scaling of the transition to parametrically driven surface waves in highly dissipative systems. *Phys. Rev. E* **55**, R3832–R3835.
- MEIJERINK, J. A. & VAN DER VORST, H. A. 1977 An iterative solution method for linear systems of which the coefficient matrix is a symmetric M-matrix. *Maths Comput.* **31**, 148–162.
- MEIJERINK, J. A. & VAN DER VORST, H. A. 1981 Guidelines for the usage of incomplete decompositions in solving sets of linear equations as they occur in practical problems. *J. Comput. Phys.* **44**, 134–155.
- MILES, J. 1993 On Faraday waves. *J. Fluid Mech.* **248**, 671–683.
- MILES, J. & HENDERSON, D. 1990 Parametrically forced surface waves. *Annu. Rev. Fluid Mech.* **22**, 143–165.
- NAYFEH, A. H. & NAYFEH, J. F. 1990 Surface waves in closed basins under principal and autoparametric resonances. *Phys. Fluids A* **2**, 1635–1648.
- NICHOLS, B. D., HIRT, C. W. & HOTCHKISS, R. S. 1980 SOLA-VOF: A solution algorithm for transient fluid flow with multiple free boundaries. *Los Alamos National Lab Rep.* LA-8355.
- OGUZ, H. N. & PROSPERETTI, A. 1990 Bubble entrainment by the impact of drops on liquid surfaces. *J. Fluid Mech.* **219**, 143–179.
- PUCKETT, E. G., ALMGREN, A. S., BELL, J. B., MARCUS, D. L. & RIDER, W. J. 1997 A high-order projection method for tracking fluid interfaces in variable density incompressible flows. *J. Comput. Phys.* **130**, 269–282.
- PUMPHREY, H. C. & CRUM, L. A. 1988 Acoustic emissions associated with drop impacts. *Sea Surface Sound.* (ed. B. R. Kerman), pp. 463–483. Kluwer.
- PUMPHREY, H. C., CRUM, L. A. & BJØRNØ, L. 1989 Underwater sound produced by individual drop impacts and rainfall. *J. Acoust. Soc. Am.* **85**, 1518–1526.
- RANGE, K., GLEZER, A. & SMITH, M. K. 2001 Vibration-induced droplet ejection from sessile drops. In preparation.
- RENARDY, Y. & RENARDY, M. 2002 PROST: a proper representation of surface tension for the volume-of-fluid method. *J. Comput. Phys.* (in press).
- RODOT, H., BISCH, C. & LASEK, A. 1979 Zero-gravity simulation of liquids in contact with a solid surface. *Acta Astronautica.* **6**, 1083–1092.
- RUDMAN, M. 1997 Volume-tracking methods for interfacial flow calculations. *Intl J. Numer. Meth. Fluids* **24**, 671–691.
- RUDMAN, M. 1999 A volume-tracking method for incompressible multifluid flows with large density variations. *Intl J. Numer. Meth. Fluids* **28**, 357–378.
- SCARDOVELLI, R. & ZALESKI, S. 1999 Direct numerical simulation of free-surface and interfacial flow. *Annu. Rev. Fluid Mech.* **31**, 567–603.
- SHI, W. T., GOODRIDGE, C. L. & LATHROP, D. P. 1997 Breaking waves: bifurcations leading to a singular wave state. *Phys. Rev. E* **56**, 4157–4161.
- SIEKMANN, J. & SCHILLING, U. 1989 On the vibrations of an inviscid liquid droplet contacting a solid wall in a low-gravity environment. *Appl. Microgravity Tech.* II **1**, 17–26.
- SOROKIN, V. I. 1957 The effect of fountain formation at the surface of a vertically oscillating liquid. *Akust. Zh.* **3**, 281–291.
- VIRNIG, J. C., BERMAN, A. S. & SETHNA, P. R. 1988 On three-dimensional nonlinear subharmonic resonant surface waves in a fluid: part II – experiment. *J. Appl. Mech.* **55**, 220–224.
- WEBSTER, D. R. & LONGMIRE, E. K. 2001 Jet pinch-off and drop formation in immiscible liquid–liquid systems. *Exps. Fluids* **30**, 47–56.
- WILKES, E. D. & BASARAN, O. A. 1997 Forced oscillations of pendant (sessile) drops. *Phys. Fluids* **9**, 1512–1528.
- WILKES, E. D. & BASARAN, O. A. 1999 Hysteretic response of supported drops during forced oscillations. *J. Fluid Mech.* **393**, 333–356.
- WILKES, E. D. & BASARAN, O. A. 2001 Drop ejection from an oscillating rod. *J. Colloid Interface Sci.* **242**, 180–201.
- WILKES, E. D., PHILLIPS, S. D. & BASARAN, O. A. 1999 Computational and experimental analysis of dynamics of drop formation. *Phys. Fluids* **11**, 3577–3598.
- YARIN, A. L. & WEISS, D. A. 1995 Impact of drops on solid surfaces: self-similar capillary waves, and splashing as a new type of kinematic discontinuity. *J. Fluid Mech.* **283**, 141–173.
- YULE, A. J. & AL-SULEIMANI, Y. 2000 On droplet formation from capillary waves on a vibrating surface. *Proc. R. Soc. Lond. A* **456**, 1069–1085.

- ZEFF, B. W., KLEBER, B., FINEBERG, J. & LATHROP, D. P. 2000 Singularity dynamics in curvature collapse and jet eruption on a fluid surface. *Nature* **403**, 401–404.
- ZHANG, W. & VINALS, J. 1997 Pattern formation in weakly damped parametric surface waves. *J. Fluid Mech.* **336**, 301–330.
- ZHANG, X. 1999*a* Dynamics of growth and breakup of viscous pendant drops into air. *J. Colloid Interface Sci.* **212**, 107–122.
- ZHANG, X. 1999*b* Dynamics of drop formation in viscous flows. *Chem. Engng Sci.* **54**, 1759–1774.